Motility-Induced Crystallization and Rotating Crystallites

Max Philipp Holl,[1,2,3,*,†] Alina Barbara Steinberg,[3*,‡] Michael te Vrugt,[4,§] and Uwe Thiele[3,5,‖]
[1]*Department of Chemistry and Materials Science, Aalto University, P.O. Box 16100, FI-00076 Aalto, Espoo 00076, Finland*
[2]*Academy of Finland Center of Excellence in Life-Inspired Hybrid Materials (LIBER), Aalto University, P.O. Box 16100, FI-00076 Aalto, Espoo 00076, Finland*
[3]*Institute of Theoretical Physics, University of Münster, Wilhelm-Klemm-Strasse 9, 48149 Münster, Germany*
[4]*Institute of Physics, Johannes Gutenberg University Mainz, 55128 Mainz, Germany*
[5]*Center for Nonlinear Science (CeNoS), University of Münster, Corrensstrasse 2, 48149 Münster, Germany*

(Received 14 August 2024; revised 28 July 2025; accepted 8 September 2025; published 6 October 2025)

Active soft matter frequently shows motility-induced phase separation, where self-propelled particles condensate into clusters with an inner liquidlike structure. Such activity may also result in motility-induced crystallization into clusters with an inner crystalline structure. We derive a higher-order active phase-field-crystal model and employ it to study the interplay of passive (i.e., thermodynamic) and active (i.e., motility-induced) condensation or evaporation and crystallization or melting. Stability and morphological phase diagrams indicate the various occurring phase coexistences and transitions, e.g., the destruction of passive clusters in the case of a density-independent effective velocity and the possible creation of active clusters in the case of a density-dependent effective velocity. Finally, simple and complex rotating crystallites are discussed, including states of time-periodic chirality.

DOI: 10.1103/m3dy-53yc

Motility-induced phase separation (MIPS) is an important focus of attention in the physics of active soft matter: when the driving activity of self-propelled particles crosses a critical density-dependent threshold the particles phase-separate into dense and dilute fluid phases even in the absence of attractive interactions. In other words they accumulate into high-density liquidlike clusters that coexist with a low-density gaslike phase [1–7]. Experimental observations [3,8–10], particle-based simulations [11–17], and continuum models mainly based on nonvariational amendments [18–23] of the Cahn-Hilliard model for phase decomposition [24] all yield consistent results for the existence and properties of such clusters [22]. Furthermore, motility can also strongly amend the phase behavior for systems that have rich phase diagrams already in the passive limit. For instance, in motility-enhanced (motility-suppressed) phase separation the parameter range where phase separation occurs is enlarged (reduced).

However, besides the clusters of liquidlike inner structure that result from phase separation, experiments and simulations also increasingly report the existence of active (or "living") crystallites, i.e., resting, traveling, or rotating particle clusters with an inner crystalline structure [8,9,12,25–30] that represent active solids [31–34] of finite size. Frequently, their dynamics is investigated using active phase-field-crystal (active PFC) models [35–43], i.e., active equivalents of the passive PFC model [44–46]—a versatile microscopic field theory for colloidal crystallization that itself is a local approximation of a dynamical density functional theory (DDFT) [47,48] and has the form of a conserved Swift-Hohenberg equation [46]. Such models are well suited to investigate activity-induced (nonequilibrium) phase transitions, multistability, time-periodic states, etc.

Although the standard active PFC model well captures the transition from resting to traveling space-filling crystalline states [35], and also predicts the existence of active crystallites in the form of resting and traveling localized states [39,42,43] it suffers from two major shortcomings: First, in the passive limit, it only describes the fluid-solid phase behavior for a single fluid phase (that is normally interpreted as liquid), but fails to capture the liquid-gas transition. Therefore, the model cannot be employed to study the interplay of condensation and crystallization. Second, it does not describe proper *motility-induced crystallization* (MIC) where activity induces crystallization. Instead, with the standard active PFC model an increase in activity tends to destroy preexisting crystalline

---

[*] These authors contributed equally to this work.
[†] Contact author: max.holl@aalto.fi
[‡] Contact author: a_stei52@uni-muenster.de
[§] Contact author: tevrugtm@uni-mainz.de
[‖] Contact author: u.thiele@uni-muenster.de; www.uwethiele.de

states [35,41,42]. In other words, the crystallization of passive (i.e., thermodynamic) crystalline clusters described by a passive PFC model [46,49] is subdued by incorporating activity that also results in the transition from resting to moving (and oscillating) crystals [41].

Here, we present a microscopically derived extended active PFC model that mitigates both shortcomings: On the one hand, in the appropriate limit it corresponds to the passive higher-order PFC model of Wang *et al.* [50] that faithfully captures phase transitions between all three phases: the liquid-gas transition between low- and high-density uniform phases as well as liquid-solid and gas-solid transitions between uniform (gas or solid) and spatially periodic (crystalline) phases. In consequence, it captures the basic phase diagram featuring gas, liquid, and solid phases including gas-liquid-solid coexistence, as well as all corresponding dynamic transitions. In contrast to the standard PFC model [44–48] its underlying free energy functional $\mathcal{F}_{\mathrm{PFC}}[\phi]$ includes contributions from three- and four-point direct correlation functions and contains derivatives of up to sixth order. A typical phase diagram in the vicinity of the triple point (three-phase coexistence) is given in Fig. 2(a) below.

On the other hand, our derivation extends the approach of [35,36] regarding activity resulting from self-propulsion. In particular, our model not only features a density-independent effective velocity [35], but additionally a microscopically justified density-dependent contribution similar to a classical MIPS model [51]. This enables our model to describe both—the destruction of passive clusters and the creation of active ones as schematically illustrated in Fig. 1. In the following, we briefly present the model, analyze its phase behavior focusing on the destruction of passive (thermodynamic) clusters, i.e., drops and crystallites, and the emergence of active ones. Finally, we analyze the emerging rotating crystallites and point out intriguing states with complex chirality dynamics.

Overall, the passive dynamics of the amended PFC model [50] in terms of the conserved density field $\phi(\mathbf{x},t)$ is nonvariationally coupled to the dynamics of a polarization field $\mathbf{P}$ that indicates the local strength and direction of polar order related to the drive of the active particles. The resulting dynamic model is

$$\partial_t\phi = \nabla^2\frac{\delta\mathcal{F}[\phi,\mathbf{P}]}{\delta\phi} - \nabla\cdot[v(\phi)\mathbf{P}], \tag{1}$$

$$\partial_t\mathbf{P} = \nabla^2\frac{\delta\mathcal{F}[\phi,\mathbf{P}]}{\delta\mathbf{P}} - D_r\frac{\delta\mathcal{F}[\phi,\mathbf{P}]}{\delta\mathbf{P}} - \nabla[\alpha v(\phi)(\phi+\rho_r)]. \tag{2}$$

Note that ϕ and temperature T are nondimensional scaled and shifted effective quantities (ρ_r is a reference density) as further detailed in Sec. A of the Supplemental Material [52], where also the full expression for the density- and polarization-dependent energy $\mathcal{F}[\phi,\mathbf{P}] = \mathcal{F}_{\mathrm{PFC}}[\phi] + \mathcal{F}_{\mathbf{P}}[\mathbf{P}]$ is given, including the dependence on T. The first and second term on the right-hand side of Eq. (2) correspond to translational and rotational diffusion, respectively. Besides these terms that represent respective conserved and nonconserved gradient dynamics, there are the active coupling terms [the respective final term of Eqs. (1) and (2)] [73]. Their nonreciprocal character breaks the overall gradient dynamics structure, i.e., represents sustained nonequilibrium influences like chemomechanical driving. They are ultimately responsible for all occurring moving and oscillating states.

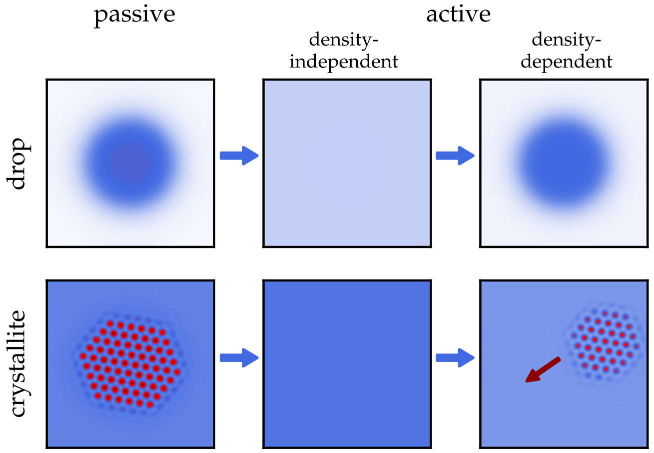

FIG. 1. A schematic illustration of the destruction of passive (thermodynamic) drops (top) and crystallites (bottom) by an increase of activity from zero (left to center), and the subsequent re-creation of both cluster types by increasing a density-dependent velocity.

The strength $v(\phi)$ of the coupling between the density and polarization represents the effective self-propulsion speed of the active particles that is often assumed constant [35,39]. In contrast, here, we have obtained the density-dependent expression $v(\phi) = v_0 - \zeta(\phi+\rho_r)$ that is widely used in effective hydrodynamic models for MIPS [19,20,23,51]. Thereby, v_0 represents an effective speed of an individual self-propelled particle while ζ results from the force imbalance related to the self-trapping due to interactions with other particles as frequently occurring at larger densities. Note that more complicated expressions [e.g., $v(\phi,\nabla^2\phi)$] may also be employed [21,23,74] but do not amend our central result. A derivation from a microscopic DDFT and a discussion of the quantitative relation to classical MIPS models [51] are provided in Secs. B and D of Supplemental Material [52], respectively.

The higher-order active PFC model (1) and (2) shows the range of behaviors sketched in Fig. 1: In the passive case ($v = 0$) the full phase behavior of a system with gas, liquid, and crystalline state is reproduced [50], shown here in Fig. 2(a) by a phase diagram in the plane spanned by effective mean density $\bar{\phi}$ and temperature T with a focus on the vicinity of the triple point at $(\bar{\phi},T)\approx(-0.5,0)$.

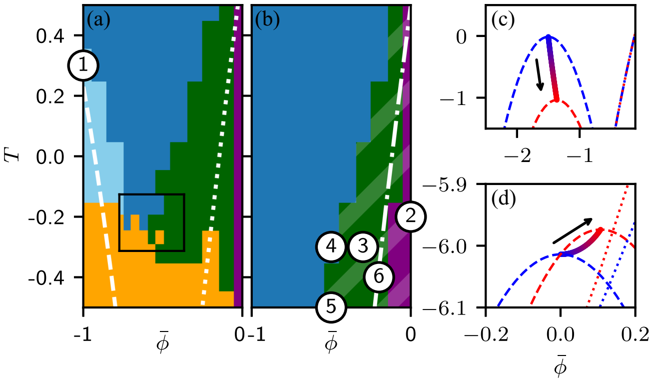

FIG. 2. Morphological phase diagrams for the extended PFC model (1) and (2) in the plane spanned by effective mean density $\bar{\phi}$ and temperature T. Shown are (a) the passive case ($v = 0$) and (b) an active case ($v_0 = 1, \zeta = 0$) with a focus on the vicinity of the triple point in the passive case [at $(\bar{\phi}, T) \approx (-0.5, 0)$] for the parameters of Ref. [50]. Time simulations are employed for finite domain size $L_x \times L_y = 100 \times 100$. Examples of occurring states at numbered loci ①-⑥ are given in Fig. 3. Dark blue indicates uniform states (gas or liquid), while light blue marks liquid-gas coexistence. Green and orange represent coexistence of a crystalline phase with liquid and gas state, respectively. The latter may also include finite-size realizations of three-phase coexistence. Finally, dark purple indicates domain-filling crystalline states. In (a) all states are at rest while in (b) moving states are shown hatched. The white dashed and dotted lines give linear stability thresholds for a Cahn-Hilliard and a conserved-Turing instability related to spinodals for phase separation and crystallization, respectively. The dot-dashed line in (b) indicates a conserved-wave instability related to the direct crystallization into moving crystals. The full set of parameters is given in Sec. A of Supplemental Material [52]. The employed parameter increments for $\bar{\phi}$ and T are both 0.1 [0.05 within the square in (a)]. Finally, panels (c) and (d) show how the spinodals change with increasing $\zeta \geq 0$ (indicated by arrows) in two qualitatively different cases. In each case, blue [red] lines indicate $\zeta = 0 [\zeta > 0]$. Specifically, (c) $v_0 = 1, \zeta = 0.2$, (d) $v_0 = 0.5$, $\zeta = 0.5$. The colored dots show the trace of the liquid-gas critical point. Specifically, in (c) ζ further suppresses phase separation for otherwise identical parameters as in (a),(b), while in (d) ζ enhances both, phase separation and crystallization (also see Sec. C of Supplemental Material [52], for remaining parameters see Table 1 of [52]).

For details on the employed time simulations see Sec. E of [52]. There is a one-phase region of uniform states (dark blue, liquid or gas), and two-phase regions of liquid-gas (light blue), solid-liquid (dark green), and solid-gas coexistence (orange). The white lines indicate linear stability thresholds for the uniform state, i.e., spinodals, with respect to liquid-gas phase separation (dashed) and crystallization (dotted). They correspond to Cahn-Hilliard (stationary, large-scale) and conserved-Turing instabilities (stationary, small-scale), respectively (see classification of Ref. [75]). Typical dispersion relations and complete spinodals are given in Sec. C of Supplemental Material [52].

Increasing the density-independent velocity v_0 (at $\zeta = 0$) from zero significantly changes the phase diagram [see Fig. 2(b)]. Overall, all clustering is reduced, the region of liquid-gas phase separation has disappeared from the shown region and crystallization is shifted toward larger densities. The dot-dashed spinodal now indicates the onset of a conserved-wave instability [75] related to the direct emergence of traveling crystalline states. The shift is consistent with the suppression of crystallization with increasing activity observed in the standard active PFC model [35,39,41]. Here, it applies as well to phase separation where with increasing v_0 the liquid-gas critical point and the spinodals are shifted toward lower temperatures. One further deduces from Fig. 2(b) that crystal-gas coexistence [yellow in Fig. 2(a)] has also shifted to similarly low values, as indicated by states ⑦ and ⑧ in Fig. 3. The remaining crystalline states all correspond to traveling states, see examples in Fig. 3. Thereby, finite-size crystallites corresponding to crystal-liquid coexistence frequently rotate as further analyzed below (also translational motion may occur). In summary, pre-existing structures that result from passive forces, i.e., by thermodynamic interactions between particles, are all counteracted by the density-independent velocity v_0.

Then, in the hatched purple region domain-filling stationary traveling crystals are found (state ①). Coexistence of drops with an extended traveling crystal has emerged (states ⑤ and ⑥). Finally, ⑦ and ⑧ provide examples of three-phase gas-liquid-solid coexistence in an active system, in the former note the liquid wetting layer at the crystal-gas interface. Note that coexisting states may also exist outside the spinodally unstable region, i.e., the borders between the colored regions in Fig. 2 represent finite-size approximations of (non)equilibrium binodals. This indicates that all transitions are of first order as also confirmed by the existence of various localized states [43,46,76]. A detailed understanding of the intricate relations between and multistability of the various uniform, periodic and localized states (that may rest or move), in particular, in the vicinity of the triple point can be achieved by considering the bifurcation structure for finite systems. A selection of corresponding results is given in Sec. F of Supplemental Material [52]. Note that in contrast to most results described for the standard active PFC model [35,39,41], here, the group velocity of the crystallites is lower than their phase velocity, i.e., individual peaks move faster than the overall structure (states ④, ⑥ to ⑧ in Fig. 3). Physically, this corresponds to particles melting at the front of the traveling crystallite into the coexisting uniform phase and crystallizing at the rear. In other words, at the rear particles get stuck in the "slowly moving traffic jam" of the crystallite, then slowly move through it until they detach themselves when reaching the front.

Interestingly, an additional density-dependent velocity of strength ζ can either further suppress clustering [see Fig. 2(c)

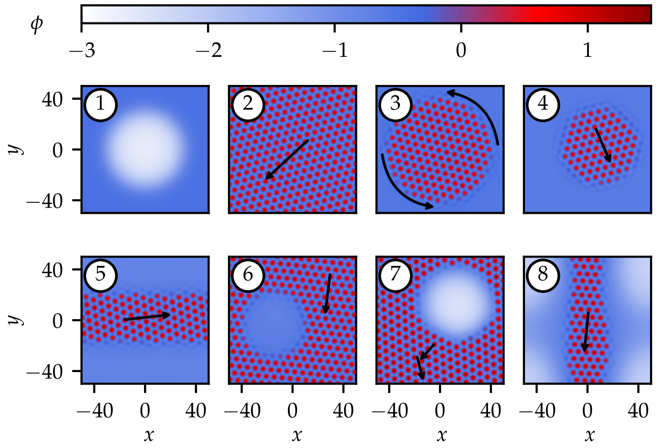

FIG. 3. Typical snapshots of various resting and moving states are represented by their density profiles $\phi(\mathbf{x}, t)$. Panels ① to ⑥ show states at parameter values indicated by corresponding numbers in Figs. 2(a) and 2(b). ⑦ and ⑧ give states with $v_0 = 1$ at $(\bar{\phi}, T) = (-0.5, -0.8)$ and $(-1, -0.58)$, respectively. Given are ① a phase-separated state of a gas bubble inside a liquid, ② an extended traveling crystal, ③ to ⑧ various types of moving crystallites. The black arrows indicate the direction of motion of the crystalline regions. Three-phase coexistence is visible in ⑦ and ⑧. A movie can be found in Supplemental Material [52].

for otherwise identical parameters as in Figs. 2(a) and 2(b)] or foster the creation of active clusters [Fig. 2(d)], also cf. Fig. 7 of Supplemental Material [52]. In the latter case an increase in ζ enhances both, phase separation and crystallization. In particular, the liquid-gas spinodal is moving to higher temperatures and densities while the liquid-crystal binodal moves to lower densities. The resulting transitions one may call MIPS and MIC. Note that in the corresponding density range our model quantitatively reproduces corresponding literature results for MIPS obtained with simpler models that do not account for crystallization as well as results for an active Cahn-Hilliard model. This is detailed in Sec. C of [52]. Note that in the case of Fig. 2(d) the resulting small distance between the critical and triple point implies that crystallites nonlinearly dominate even in part of the phase-separation region.

An intriguing state are rotating crystallites as state ③ in Fig. 3. Such states are described for many experimental systems [27,32,77–80] and particle-based simulations [15,81], both for chiral [29,78,81] and nonchiral [15,32,82,83] particles. However, such states are rarely mentioned in studies employing PFC models ([38] shows their existence for a circular domain). Here, they frequently occur beside the also found traveling crystallites (state ④ in Fig. 3). On general grounds, both should be expected even for nonchiral particles as the corresponding collective motions result from the interaction of pitchfork bifurcations with Goldstone modes related to homogeneity and isotropy of space, respectively. Such drift- and rotation-pitchfork bifurcations were studied e.g., for a reaction-diffusion system [84].

Here, the simplest rotating crystalline clusters move as a nearly hexagonal rigid body, i.e., with identical group and phase velocity. Figure 4 provides an overview of their characteristics. Their radius R and angular velocity ω are given as a function of T and R, respectively, at several fixed densities $\bar{\phi} = -0.2 \ldots -0.45$. The dependence $R(T)$ has the appearance of a staircase that goes up with decreasing T while the steps are getting longer (at equal height), a typical behavior for localized states that show homoclinic snaking [85,86]. Figure 4 focuses on localized states with a central peak, though states with a central hole also exist and show a similar stairlike behavior. Inspecting profiles like Figs. 4(c) and 4(d) shows that along each of the nearly horizontal parts an initially incomplete outer shell of the hexagonal structure laterally grows more peaks with decreasing T. When a shell is completed, a new outer layer is initiated by peaks in the central part of each face that then grows, thereby resulting in the steplike increase of R. In other words, each step corresponds to a stable radius. A corresponding structure is visible in the dependence of ω on R [Fig. 4(b)] where for small clusters the velocity decreases with increasing cluster size while at large R one can discern a very small increase. Beside the shown clusters of overall sixfold symmetry, also less symmetric states exist that feature facets of different lengths (not shown). Further note that for the employed domain size, clusters above $R_{\max} \approx 45.3$ interact via the boundaries, ultimately form other states, and are therefore excluded from the analysis. Similarly, there is a minimal radius $R_{\min} \approx 13.7$ corresponding to the smallest stable cluster (two layers around the central peak). Lower densities result in uniform states [87].

At more extreme conditions, e.g., lower temperature and larger density with $\zeta > 0$ and $\rho_r = 3$ more intricate behavior is observed: There, also a stripe phase exists (as in standard PFC models [35,46]) that corresponds to particles that are periodically placed in one direction but are mobile in the other one. This results in the new types of localized states shown in Fig. 5. They are often of lower symmetry and either combine local stripe and crystalline arrangements [two-phase cluster, Figs. 5(c)–5(g)] or predominantly consist of localized stripe phase [Figs. 5(b) and 5(h)]. Because of the activity the entire clusters and their parts may move in different ways. A recurring type of movement is the swinging motion found in Figs. 5(a), 5(b), and 5(e). Such a pattern of time-periodic chirality is reminiscent of a torsion pendulum and implies a periodic reversal in the polarization field. It can also be found in experiments, e.g., see Ref. [77]. Other motion types which mostly involve the stripe phase resemble bouncing [Fig. 5(c)], waving [Figs. 5(b) and (5e)] and wobbling [Figs. 5(c)–5(e) and 5(g)], see movie in Supplemental Material [52]. In experiments or simulations such states

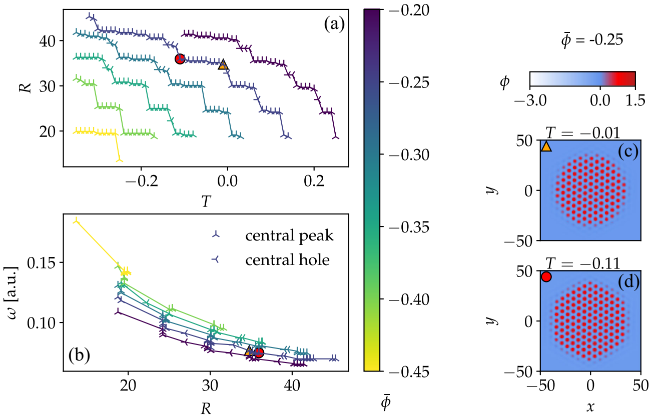

FIG. 4. Characteristics of rotating crystallites for the case of $v_0 = 1$ and $\zeta = 0$. Shown are (a) the radius R in dependence of the temperature T and (b) the angular velocity ω (in degree per time unit) as a function of R, both at several fixed mean densities $\bar{\phi}$ as indicated by the color bar. Panels (c) and (d) show profiles of states at the two ends of a single plateau at $\bar{\phi} = -0.25$ in (a) where they are marked by an orange triangle and red circle, respectively. The domain size is $L_x = L_y = 100$, for numerical details see Sec. E of Supplemental Material [52].

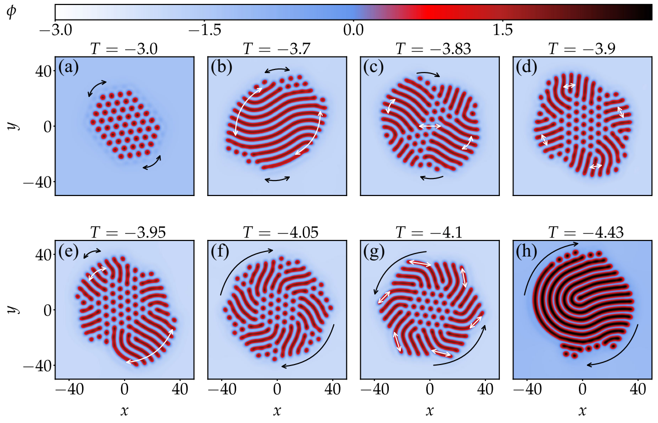

FIG. 5. Intricate chiral behavior of active crystalline clusters at $\bar{\phi} = -1$ and rather low T (as given at the panels). Black and white arrows indicate main overall and inner modi of motion, respectively, and ϕ is given by the color bar. The individual states are described in the main text and Supplemental Material [52] where also a movie is given. Remaining parameters are $\zeta = 1$ and $\rho_r = 3$.

would correspond to clusters with a rigid core structure and a less rigid but still crystalline outer part. Figure 4(b) of [80] shows some promising candidates. There, time traces visualize particle motion, i.e., their large lower left cluster combines strongly and weakly moving particles in the same crystallite, suggesting that some of them are stronger bound to their position than others, and further clusters show wavy time traces. This suggests modes of relative motion as seen in our Fig. 5.

To conclude, we have presented an amended active phase-field-crystal model capable of describing (active) gas, liquid and solid phases, including their dynamics in the vicinity of the triple point. This has allowed us to study the interplay of passive and active condensation and crystallization including phase coexistences. This includes a variety of traveling and rotating crystallites, i.e., finite-size active solids, that may coexist with gas or liquid as further evidenced by phase diagrams and a detailed study of rotating crystallites. States with time-periodic chirality, i.e., direction-reversing rotational waves, have also been described.

Phase diagrams obtained with the present continuum approach qualitatively match results of particle-based simulations, see, e.g., Refs. [16,17] (when accounting for their nondimensionalization), even though their models are for hard spheres [88]. Studies with softer attractive particles should identify the destruction of passive clusters and creation of active ones as well in particle-based simulations and experiments. Incorporating the approach of [89], the model may also be extended toward spinning particles with resulting effective interactions [78]. Finally, note that the presented conceptually relatively simple continuum model may be adapted to study many effects that involve active solid, liquid, and gas phase as phenomena of nonequilibrium pattern formation. Examples include wetting phenomena on active solids, nucleation processes for active crystals and premelting transitions at grain boundaries of active solids.

Acknowledgments—We acknowledge usage of the HPC cluster PALMA II of the University of Münster, subsidized by the DFG (No. INST 211/667-1). M. t. V. is funded by the Deutsche Forschungsgemeinschaft (DFG, German Research Foundation)—SFB 1551, Project-ID 464588647.

Data availability—The data that support the findings of this article are openly available [90].

[1] S. Ramaswamy, The mechanics and statistics of active matter, Annu. Rev. Condens. Matter Phys. **1**, 323 (2010).
[2] P. Romanczuk, M. Bär, W. Ebeling, B. Lindner, and L. Schimansky-Geier, Active Brownian particles from individual to collective stochastic dynamics, Eur. Phys. J. Spec. Top. **202**, 1 (2012).
[3] M. C. Marchetti, J. F. Joanny, S. Ramaswamy, T. B. Liverpool, J. Prost, M. Rao, and R. A. Simha, Hydrodynamics of soft active matter, Rev. Mod. Phys. **85**, 1143 (2013).
[4] M. E. Cates and J. Tailleur, Motility-induced phase separation, Annu. Rev. Condens. Matter Phys. **6**, 219 (2015).
[5] D. Marenduzzo, An introduction to the statistical physics of active matter: Motility-induced phase separation and the "generic instability" of active gels, Eur. Phys. J. Spec. Top. **225**, 2065 (2016).
[6] G. Gompper *et al.*, The 2020 motile active matter roadmap, J. Phys. Condens. Matter **32**, 193001 (2020).

[7] M. R. Shaebani, A. Wysocki, R. G. Winkler, G. Gompper, and H. Rieger, Computational models for active matter, Nat. Rev. Phys. **2**, 181 (2020).

[8] I. Buttinoni, J. Bialké, F. Kümmel, H. Löwen, C. Bechinger, and T. Speck, Dynamical clustering and phase separation in suspensions of self-propelled colloidal particles, Phys. Rev. Lett. **110**, 238301 (2013).

[9] C. Bechinger, R. Di Leonardo, H. Löwen, C. Reichhardt, G. Volpe, and G. Volpe, Active particles in complex and crowded environments, Rev. Mod. Phys. **88**, 045006 (2016).

[10] A. A. Fragkopoulos, J. Vachier, J. Frey, F.-M. Le Menn, M. G. Mazza, M. Wilczek, D. Zwicker, and O. Bäumchen, Self-generated oxygen gradients control collective aggregation of photosynthetic microbes, J. R. Soc. Interface **18**, 20210553 (2021).

[11] F. D. C. Farrell, M. C. Marchetti, D. Marenduzzo, and J. Tailleur, Pattern formation in self-propelled particles with density-dependent motility, Phys. Rev. Lett. **108**, 248101 (2012).

[12] B. M. Mognetti, A. Saric, S. Angioletti-Uberti, A. Cacciuto, C. Valeriani, and D. Frenkel, Living clusters and crystals from low-density suspensions of active colloids, Phys. Rev. Lett. **111**, 245702 (2013).

[13] A. Patch, D. Yllanes, and M. C. Marchetti, Kinetics of motility-induced phase separation and swim pressure, Phys. Rev. E **95**, 012601 (2017).

[14] E. Crosato, M. Prokopenko, and R. E. Spinney, Irreversibility and emergent structure in active matter, Phys. Rev. E **100**, 042613 (2019).

[15] L. Caprini, U. Marini Bettolo Marconi, and A. Puglisi, Spontaneous velocity alignment in motility-induced phase separation, Phys. Rev. Lett. **124**, 078001 (2020).

[16] F. Turci and N. B. Wilding, Phase separation and multibody effects in three-dimensional active Brownian particles, Phys. Rev. Lett. **126**, 038002 (2021).

[17] A. K. Omar, K. Klymko, T. GrandPre, and P. L. Geissler, Phase diagram of active Brownian spheres: Crystallization and the metastability of motility-induced phase separation, Phys. Rev. Lett. **126**, 188002 (2021).

[18] R. Wittkowski, A. Tiribocchi, J. Stenhammar, R. J. Allen, D. Marenduzzo, and M. E. Cates, Scalar ϕ^4 field theory for active-particle phase separation, Nat. Commun. **5**, 4351 (2014).

[19] T. Speck, J. Bialké, A. M. Menzel, and H. Löwen, Effective Cahn-Hilliard equation for the phase separation of active Brownian particles, Phys. Rev. Lett. **111**, 218304 (2014).

[20] T. Speck, A. M. Menzel, J. Bialké, and H. Löwen, Dynamical mean-field theory and weakly non-linear analysis for the phase separation of active Brownian particles, J. Chem. Phys. **142**, 224109 (2015).

[21] L. Rapp, F. Bergmann, and W. Zimmermann, Systematic extension of the Cahn-Hilliard model for motility-induced phase separation, Eur. Phys. J. E **42**, 57 (2019).

[22] J. Bickmann and R. Wittkowski, Predictive local field theory for interacting active Brownian spheres in two spatial dimensions, J. Phys. Condens. Matter **32**, 214001 (2020).

[23] J. Bickmann and R. Wittkowski, Collective dynamics of active Brownian particles in three spatial dimensions: A predictive field theory, Phys. Rev. Res. **2**, 033241 (2020).

[24] A. J. Bray, Theory of phase-ordering kinetics, Adv. Phys. **43**, 357 (1994).

[25] I. Theurkauff, C. Cottin-Bizonne, J. Palacci, C. Ybert, and L. Bocquet, Dynamic clustering in active colloidal suspensions with chemical signaling, Phys. Rev. Lett. **108**, 268303 (2012).

[26] J. Palacci, S. Sacanna, A. P. Steinberg, D. J. Pine, and P. M. Chaikin, Living crystals of light-activated colloidal surfers, Science **339**, 936 (2013).

[27] A. P. Petroff, X.-L. Wu, and A. Libchaber, Fast-moving bacteria self-organize into active two-dimensional crystals of rotating cells, Phys. Rev. Lett. **114**, 158102 (2015).

[28] A. Zöttl and H. Stark, Emergent behavior in active colloids, J. Phys. Condens. Matter **28**, 253001 (2016).

[29] A. P. Petroff and A. Libchaber, Nucleation of rotating crystals by Thiovulum majus bacteria, New J. Phys. **20**, 015007 (2018).

[30] F. Ginot, I. Theurkauff, F. Detcheverry, C. Ybert, and C. Cottin-Bizonne, Aggregation-fragmentation and individual dynamics of active clusters, Nat. Commun. **9**, 696 (2018).

[31] R. J. Hawkins and T. B. Liverpool, Stress reorganization and response in active solids, Phys. Rev. Lett. **113**, 028102 (2014).

[32] C. Hernández-López, P. Baconnier, C. Coulais, O. Dauchot, and G. Düring, Model of active solids: Rigid body motion and shape-changing mechanisms, Phys. Rev. Lett. **132**, 238303 (2024).

[33] E. Ferrante, A. E. Turgut, M. Dorigo, and C. Huepe, Elasticity-based mechanism for the collective motion of self-propelled particles with springlike interactions: A model system for natural and artificial swarms, Phys. Rev. Lett. **111**, 268302 (2013).

[34] A. Maitra and S. Ramaswamy, Oriented active solids, Phys. Rev. Lett. **123**, 238001 (2019).

[35] A. M. Menzel and H. Löwen, Traveling and resting crystals in active systems, Phys. Rev. Lett. **110**, 055702 (2013).

[36] A. M. Menzel, T. Ohta, and H. Löwen, Active crystals and their stability, Phys. Rev. E **89**, 022301 (2014).

[37] A. I. Chervanyov, H. Gomez, and U. Thiele, Effect of the orientational relaxation on the collective motion of patterns formed by self-propelled particles, Europhys. Lett. **115**, 68001 (2016).

[38] F. Alaimo, S. Praetorius, and A. Voigt, A microscopic field theoretical approach for active systems, New J. Phys. **18**, 083008 (2016).

[39] L. Ophaus, S. V. Gurevich, and U. Thiele, Resting and traveling localized states in an active phase-field-crystal model, Phys. Rev. E **98**, 022608 (2018).

[40] S. Praetorius, A. Voigt, R. Wittkowski, and H. Löwen, Active crystals on a sphere, Phys. Rev. E **97**, 052615 (2018).

[41] L. Ophaus, J. Kirchner, S. V. Gurevich, and U. Thiele, Phase-field-crystal description of active crystallites: Elastic and inelastic collisions, Chaos **30**, 123149 (2020).

[42] L. Ophaus, E. Knobloch, S. V. Gurevich, and U. Thiele, Two-dimensional localized states in an active phase-field-crystal model, Phys. Rev. E **103**, 032601 (2021).

[43] M. P. Holl, A. J. Archer, S. V. Gurevich, E. Knobloch, L. Ophaus, and U. Thiele, Localized states in passive and active phase-field-crystal models, IMA J. Appl. Math. **86**, 896 (2021).

[44] K. R. Elder, M. Katakowski, M. Haataja, and M. Grant, Modeling elasticity in crystal growth, Phys. Rev. Lett. **88**, 245701 (2002).

[45] H. Emmerich, H. Löwen, R. Wittkowski, T. Gruhn, G. I. Tóth, G. Tegze, and L. Gránásy, Phase-field-crystal models for condensed matter dynamics on atomic length and diffusive time scales: An overview, Adv. Phys. **61**, 665 (2012).

[46] U. Thiele, A. J. Archer, M. J. Robbins, H. Gomez, and E. Knobloch, Localized states in the conserved Swift-Hohenberg equation with cubic nonlinearity, Phys. Rev. E **87**, 042915 (2013).

[47] A. J. Archer, D. J. Ratliff, A. M. Rucklidge, and P. Subramanian, Deriving phase field crystal theory from dynamical density functional theory: Consequences of the approximations, Phys. Rev. E **100**, 022140 (2019).

[48] M. te Vrugt, H. Löwen, and R. Wittkowski, Classical dynamical density functional theory: From fundamentals to applications, Adv. Phys. **69**, 121 (2020).

[49] P. Subramanian, A. J. Archer, E. Knobloch, and A. M. Rucklidge, Spatially localized quasicrystalline structures, New J. Phys. **20**, 122002 (2018).

[50] Z.-L. Wang, Z. Liu, Z.-F. Huang, and W. Duan, Minimal phase-field crystal modeling of vapor-liquid-solid coexistence and transitions, Phys. Rev. Mater. **4**, 103802 (2020).

[51] J. Bialké, H. Löwen, and T. Speck, Microscopic theory for the phase separation of self-propelled repulsive disks, Europhys. Lett. **103**, 30008 (2013).

[52] See Supplemental Material at http://link.aps.org/supplemental/10.1103/m3dy-53yc for details on the underlying energy functional, governing equations and parameters, a microscopic derivation of the model, a linear stability analysis of uniform states, a discussion of the quantitative relation to classical MIPS and active Cahn-Hilliard models, details on the used numerical methods, and an analysis of the bifurcation behavior for one-dimensional states. It also includes Refs. [53–72].

[53] J. P. Boyd, *Chebyshev and Fourier Spectral Methods* (Dover Publ., Mineola, NY, 2. (rev.) edition, 2001).

[54] S. Engelnkemper, S. V. Gurevich, H. Uecker, D. Wetzel, and U. Thiele, Continuation for thin film hydrodynamics and related scalar problems, in *Computational Modeling of Bifurcations and Instabilities in Fluid Mechanics*, edited by A. Gelfgat, Computational Methods in Applied Sciences Vol. 50 (Springer, Cham, 2019), pp. 459–501, 10.1007/978-3-319-91494-7_13.

[55] H. Uecker, D. Wetzel, and J. D. M. Rademacher, PDE2PATH—a Matlab package for continuation and bifurcation in 2D elliptic systems, Numer. Math. Theory Methods Appl. **7**, 58 (2014).

[56] D. Greve and U. Thiele, An amplitude equation for the conserved-Hopf bifurcation—derivation, analysis, and assessment, Chaos **34**, 123134 (2024).

[57] G. S. Redner, M. F. Hagan, and A. Baskaran, Structure and dynamics of a phase-separating active colloidal fluid, Phys. Rev. Lett. **110**, 055701 (2013).

[58] M. te Vrugt and R. Wittkowski, Relations between angular and Cartesian orientational expansions, AIP Adv. **10**, 035106 (2020).

[59] M. te Vrugt, J. Bickmann, and R. Wittkowski, How to derive a predictive field theory for active Brownian particles: A step-by-step tutorial, J. Phys. Condens. Matter **35**, 313001 (2023).

[60] M. te Vrugt, M. P. Holl, A. Koch, R. Wittkowski, and U. Thiele, Derivation and analysis of a phase field crystal model for a mixture of active and passive particles, Modelling Simul. Mater. Sci. Eng. **30**, 084001 (2022).

[61] S. Hermann, P. Krinninger, D. de las Heras, and M. Schmidt, Phase coexistence of active Brownian particles, Phys. Rev. E **100**, 052604 (2019).

[62] Z.-F. Huang, M. te Vrugt, R. Wittkowski, and H. Löwen, Active pattern formation emergent from single-species nonreciprocity, arXiv:2404.10093.

[63] Z.-F. Huang, M. te Vrugt, R. Wittkowski, and H. Löwen, Anomalous grain dynamics and grain locomotion of odd crystals, arXiv:2505.03957 [Proc. Natl. Acad. Sci. U.S.A. (to be published)].

[64] R. Wittkowski, J. Stenhammar, and M. E. Cates, Nonequilibrium dynamics of mixtures of active and passive colloidal particles, New J. Phys. **19**, 105003 (2017).

[65] S. Bröker, M. te Vrugt, J. Jeggle, J. Stenhammar, and R. Wittkowski, Pair-distribution function of active Brownian spheres in three spatial dimensions: Simulation results and analytical representation, Soft Matter **20**, 224 (2024).

[66] S. Bröker, M. te Vrugt, and R. Wittkowski, Collective dynamics and pair-distribution function of active Brownian ellipsoids in two spatial dimensions, Commun. Phys. **7**, 238 (2024).

[67] J. Jeggle, J. Stenhammar, and R. Wittkowski, Pair-distribution function of active Brownian spheres in two spatial dimensions: Simulation results and analytic representation, J. Chem. Phys. **152**, 194903 (2020).

[68] U. Marini Bettolo Marconi and P. Tarazona, Dynamic density functional theory of fluids, J. Chem. Phys. **110**, 8032 (1999).

[69] A. J. Archer and R. Evans, Dynamical density functional theory and its application to spinodal decomposition, J. Chem. Phys. **121**, 4246 (2004).

[70] A. J. M. Yang, P. D. Fleming, and J. H. Gibbs, Molecular theory of surface tension, J. Chem. Phys. **64**, 3732 (1976).

[71] J. Toner and Y. Tu, Long-range order in a two-dimensional dynamical XY model: How birds fly together, Phys. Rev. Lett. **75**, 4326 (1995).

[72] M. P. Holl, A. J. Archer, and U. Thiele, Efficient calculation of phase coexistence and phase diagrams: Application to a binary phase-field crystal model, J. Phys. Condens. Matter **33**, 115401 (2021).

[73] The constant α allows one to easily switch between common parametrizations.

[74] M. E. Cates and J. Tailleur, When are active Brownian particles and run-and-tumble particles equivalent? Consequences for motility-induced phase separation, Europhys. Lett. **101**, 20010 (2013).

[75] T. Frohoff-Hülsmann and U. Thiele, Nonreciprocal Cahn-Hilliard model emerges as a universal amplitude equation, Phys. Rev. Lett. **131**, 107201 (2023).

[76] U. Thiele, T. Frohoff-Hülsmann, S. Engelnkemper, E. Knobloch, and A. J. Archer, First order phase transitions and the thermodynamic limit, New J. Phys. **21**, 123021 (2019).

[77] H. Xu, Y. Huang, R. Zhang, and Y. Wu, Autonomous waves and global motion modes in living active solids, Nat. Phys. **19**, 46 (2023).

[78] T. H. Tan, A. Mietke, J. Li, Y. Chen, H. Higinbotham, P. J. Foster, S. Gokhale, J. Dunkel, and N. Fakhri, Odd dynamics of living chiral crystals, Nature (London) **607**, 287 (2022).

[79] J. Yan, S. C. Bae, and S. Granick, Rotating crystals of magnetic Janus colloids, Soft Matter **11**, 147 (2015).

[80] M. N. van der Linden, L. C. Alexander, D. G. A. L. Aarts, and O. Dauchot, Interrupted motility induced phase separation in aligning active colloids, Phys. Rev. Lett. **123**, 098001 (2019).

[81] N. H. P. Nguyen, D. Klotsa, M. Engel, and S. C. Glotzer, Emergent collective phenomena in a mixture of hard shapes through active rotation, Phys. Rev. Lett. **112**, 075701 (2014).

[82] Z. T. Liu, Y. Shi, Y. Zhao, H. Chaté, X.-q. Shi, and T. H. Zhang, Activity waves and freestanding vortices in populations of subcritical Quincke rollers, Proc. Natl. Acad. Sci. U.S.A. **118**, e2104724118 (2021).

[83] B. V. Hokmabad, A. Nishide, P. Ramesh, C. Krüger, and C. C. Maass, Spontaneously rotating clusters of active droplets, Soft Matter **18**, 2731 (2022).

[84] A. S. Moskalenko, A. W. Liehr, and H. G. Purwins, Rotational bifurcation of localized dissipative structures, Europhys. Lett. **63**, 361 (2003).

[85] J. Burke and E. Knobloch, Localized states in the generalized Swift-Hohenberg equation, Phys. Rev. E **73**, 056211 (2006).

[86] E. Knobloch, Localized structures and front propagation in systems with a conservation law, IMA J. Appl. Math. **81**, 457 (2016).

[87] At mean densities higher than $\bar{\phi} = -0.45$, one finds a larger $R_{\min} \approx 18.8$ due to the softening of the interface between uniform background and pattern. The interface is quite sharp at low T but widens at larger T.

[88] That their simulations do not show traveling crystallites may be due to their choice of boundary conditions.

[89] Z. F. Huang, A. M. Menzel, and H. Löwen, Dynamical crystallites of active chiral particles, Phys. Rev. Lett. **125**, 218002 (2020).

[90] M. P. Holl, A. B. Steinberg, M. te Vrugt, and U. Thiele, Data supplement for "Motility-induced crystallization and rotating crystallites", Zenodo, 2025, 10.5281/zenodo.17104279.

Supplementary Material - Motility-induced crystallization and rotating crystallites

Max Philipp Holl,[1, 2, 3, *] Alina Barbara Steinberg,[3, †] Michael te Vrugt,[4, ‡] and Uwe Thiele[3, 5, §]
[1]*Department of Chemistry and Materials Science,*
Aalto University, P.O. Box 16100, FI-00076 Aalto, Finland
[2]*Academy of Finland Center of Excellence in Life-Inspired Hybrid Materials (LIBER),*
Aalto University, P.O. Box 16100, FI-00076 Aalto, Finland
[3]*Institute of Theoretical Physics, University of Münster,*
Wilhelm-Klemm-Str. 9, 48149 Münster, Germany
[4]*Institute of Physics, Johannes Gutenberg University Mainz, 55128 Mainz, Germany*
[5]*Center for Nonlinear Science (CeNoS), University of Münster, Corrensstr. 2, 48149 Münster, Germany*

SUPPLEMENTARY MATERIAL

The Supplementary Material provides further details and background information regarding the higher-order active Phase-Field-Crystal (PFC) model presented and analyzed in the main text published as M. Holl et al., *Phys. Rev. Lett.* (2025), doi:10.1103/m3dy-53yc). In particular, section A gives details for the active PFC model, namely, the employed energy functional, the specific kinetic equations, and the complete set of parameters. Furthermore, it gives the parameters of the accompanying movies and briefly discusses their content. Then, section B sketches a derivation of the PFC model from a microscopic model including a discussion of important differences to the literature. Subsequently, section E details the employed numerical methods and related parameters while section C presents the linear stability analysis of uniform states, discusses the types of resulting dispersion relations and the corresponding spinodals and their dependence on parameters. This is expanded in section D by a detailed description of the relation of the studied PFC model to limiting cases, namely, an active Cahn-Hilliard model and a standard MIPS model. Finally, section F discusses the intricate bifurcation structure of uniform, periodic, and localized states in the case of one-dimensional domains that in conjunction with the phase diagrams in the main text allows for a deeper understanding of the system behavior.

A. Energy functional, governing equations and parameters

First, we provide details on the employed energy functional $\mathcal{F}[\phi, \mathbf{P}]$ underlying the gradient dynamics in Eqs. (1) and (2) of the main text and the specific employed parameter values. The order parameter field $\phi(\mathbf{x}, t)$ follows a mass-conserving dynamics and represents a nondimensional effective density, namely, a shifted particle number density ρ. Specifically, $\phi = \rho - \rho_r$. For ease of comparison, the reference density ρ_r is chosen such that $\phi = 0$ corresponds to the critical point of the standard PFC model (without liquid-gas transition), cf. [1, 2]. Note that there are two common interpretations of the peaks in ϕ in the crystalline structures: As the density field in a field theory represents the probability of finding a particle at a certain position one may either see a peak as representing a single particle (that fluctuates about the central point of the peak), e.g., a single hard-sphere colloidal particle, or, alternatively, as a group of particles, e.g., for star-shaped polymers where several can 'sit on top of each other.' The correct interpretation depends on the studied system and the underlying classical Density Functional Theory model that the PFC model approximates, see e.g., the comprehensive overview of PFC modeling in [3] and the discussion of various levels of approximation in [4]. As PFC models correspond to generic approximations of lowest order, the distinction between the different interpretations only matters when discussing specifics of the observed phases.

The free energy functional $\mathcal{F}[\phi, \mathbf{P}]$ combines the density-dependent higher-order free energy $\mathcal{F}_{\mathrm{PFC}}[\phi]$ developed by Wang *et al.* [5] and an orientational part $\mathcal{F}_{\mathbf{P}}[\mathbf{P}]$. The latter is chosen identical to the corresponding part of the energy for the standard active PFC model [1, 2, 6]. Overall we have

$$\mathcal{F}[\phi, \mathbf{P}] = \mathcal{F}_{\mathrm{PFC}}[\phi] + \mathcal{F}_{\mathbf{P}}[\mathbf{P}]. \tag{1}$$

The density-dependent part is

$$\begin{aligned}\mathcal{F}_{\mathrm{PFC}}[\phi] = \int & -B_0(T)\phi - \frac{1}{2}\phi\left(C_0(T) + C_2(T)\Delta + C_4(T)\Delta^2 + C_6\Delta^3\right)\phi \\ & - \frac{1}{6}\left[D_0\phi^3 + D_{11}\phi^2\Delta\phi\right] - \frac{1}{24}\left\{E_0\phi^4 + E_{1122}\phi^2[\Delta\phi]^2\right\} \mathrm{d}^n r \qquad (2)\\ = \int & f_{\mathrm{PFC}}\, \mathrm{d}^n r\,. \qquad (3)\end{aligned}$$

where we explicitly indicate the temperature dependencies of the various coefficients as carefully developed in [5] such that a standard solid-liquid-gas phase diagram is reproduced in the plane spanned by mean density $\bar{\phi}$ and effective temperature T. The latter is scaled and shifted in such a way that in the passive case the triple point is at $T = 0$ and the critical point of the liquid-gas transition is at $T = 1$. Furthermore, Δ is the Laplace operator and n the spatial dimension. For the sake of comparison, the employed T-dependencies of coefficients B_0, C_0, C_2, and C_4 and all related parameters are chosen as in [5] for most of our work, and given in Table I. The higher-order terms $D_{11}\phi^2(\mathbf{r})\Delta\phi(\mathbf{r})$ and $E_{1122}\phi^2(\mathbf{r})[\Delta\phi(\mathbf{r})]^2$ stem from three- and four-point correlations, respectively, and are essential to obtain the correct sequence of phase transitions. For nonzero D_{11}, one needs $E_{1122} < 0$ to prevent divergent large-k behavior at very large mean densities $\bar{\phi}$.

TABLE I. Parameters and functional dependencies used in the free energy $\mathcal{F}_{\mathrm{PFC}}[\phi]$ of the passive PFC model as determined in Ref. [5]. In particular, B_0, C_0, C_2, and C_4 all depend on the effective temperature T.

used in	B_0	C_0	C_2	C_4	C_6	D_0	D_{11}	E_0	E_{1122}
Ref. [5] Fig. 2 (a)-(c), 3-5 of main text Fig. 1, 2, 4-7 of SM	-4.5 $-3T$	-5.764 $-T$	17.8 $+2T$	39.8 $-T$	16	-9	-34.2	-6	-52.1
Fig. 2 (d) of main text	-4.5 $-3T$	-5.764 $-T$	17.8 $+2T$	39.8 $-T$	200	0	-34.2	-6	-52.1

The polarization-dependent part is [1]

$$\mathcal{F}_{\mathbf{P}}[\mathbf{P}] = \int \frac{D_c}{2}\mathbf{P}^2 + \frac{a}{4}\mathbf{P}^4 \mathrm{d}^n r. \tag{4}$$

For $D_c < 0$ and $a > 0$ it allows for spontaneous polarization. However, we follow most earlier analyses [1, 2, 6] and simply use $a = 0$. For D_c we use $D_c = 0.2$. Introducing the free energy Eq. (1) into the kinetic equations Eqs. (1) and (2) of the main text we obtain

$$\begin{aligned}\partial_t\phi = \Delta\Big\{ &-(C_0(T) + C_2(T)\Delta + C_4(T)\Delta^2 + C_6\Delta^3)\phi - \frac{1}{2}D_0\phi^2 - \frac{1}{6}D_{11}(2\phi\Delta\phi + \Delta(\phi^2)) \\ &-\frac{1}{6}E_0\phi^3 - \frac{1}{12}E_{1122}[\phi(\Delta\phi)^2 + \Delta(\phi^2\Delta\phi)]\Big\} - \nabla\cdot[v(\phi)\mathbf{P}], \qquad (5)\\ \partial_t\mathbf{P} = D_c\Delta\mathbf{P} &- D_{nc}\mathbf{P} - \nabla\cdot[\alpha v(\phi)(\phi + \rho_r)]. \qquad (6)\end{aligned}$$

Further, we set the mobility constants for the conserved and the nonconserved part of the polarization dynamics to $D_{nc} = D_r D_c = 0.5$ which corresponds to rotational diffusion of the polarization. The constant α in the coupling term is not a physical parameter but can be employed to switch between different parameterizations employed in different parts of the literature. Here, it is fixed to $\alpha = 0.5$ as in models for motility-induced phase separation, e.g., Ref. [7]. Alternatively, $\alpha = 1$ would be the value employed in standard active PFC models [1, 2]. However, the influence of the qualitative behavior is small. The specific chosen parameters in $v = v_0 - \zeta(\phi + \rho_r)$ are given in the main text. A microscopic derivation of the amended active PFC model is given in Sec. B of this SM, while the relation of the appropriate limiting cases to models for motility-induced phase separation (MIPS) [8] is discussed in section D.

In the passive limit, Eqs. (5) and (6) decouple and steady states (with $\partial_t\phi = 0$) are obtained by solving the twice integrated Eq. (5), i.e.,

$$\begin{aligned}0 = &-(C_0(T) + C_2(T)\Delta + C_4(T)\Delta^2 + C_6\Delta^3)\phi - \frac{1}{2}D_0\phi^2 - \frac{1}{6}D_{11}(2\phi\Delta\phi + \Delta(\phi^2)) \\ &- \frac{1}{6}E_0\phi^3 - \frac{1}{12}E_{1122}[\phi(\Delta\phi)^2 + \Delta(\phi^2\Delta\phi)] - \tilde{\mu}.\end{aligned} \tag{7}$$

The integration constant $\tilde{\mu}$ is related to the chemical potential μ by $\tilde{\mu} = B_0 + \mu$. Note that the constant of the first integration is set to zero as there is no flux across the domain boundaries. Equilibrium steady states described by Eq. (7) may be followed through parameter space employing numerical path continuation while the dynamics described by Eqs. (5) and (6) can be studied employing numerical time integration. Information on the numerical methods is given in section E.

The movie 'eaPFC-fig3-video.avi' accompanying Fig. 3 of the main text uses $\zeta = 0$ for all panels. Panel ① at $\bar{\phi} = -1$, $T = 0.3$ and $v_0 = 0$ shows a state with liquid-gas phase separation. For all remaining panels we use $v_0 = 1$. Panel ② at $\bar{\phi} = 0$ and $T = -0.2$ shows a domain-filling traveling crystal. Panels ③ and ④ show at $T = -0.3$ rotating ($\bar{\phi} = -0.3$) and traveling ($\bar{\phi} = -0.5$) localized states, respectively. Panel ⑤ shows a nearly horizontal slap-like extended traveling crystal coexisting with a liquid at $\bar{\phi} = -0.2$ and $T = -0.4$. Note that in panel ④ group and phase velocity are not identical, i.e., the cluster moves at a slower speed than the individual crystallized particles. This is a typical traffic-jam effect: particles arive at its back end, move through the jam (the cluster), and finally detach at the front. Similar effects are as well seen in panels ⑥ to ⑧. In particular, panel ⑥ shows an extended traveling crystal coexisting with a slowly downward moving hole filled by the fluid phase at $\bar{\phi} = -0.5$ and $T = -0.5$, panel ⑦ and ⑧ show three-phase coexistence of extended traveling crystals with both gas and a fluid phase at $(\bar{\phi}, T) = (-0.5, -0.8)$ and $(-1, -0.58)$, respectively (in ⑦ in the form of a wetting layer at the crystal-gas interface around a gas filled cavity). Interestingly, in panel ⑦ the traveling crystal moves in an undulating manner.

The movie 'eaPFC-fig5-video.avi' accompanying Fig. 5 of the main text illustrates the dynamic chiral behavior of active crystalline clusters at $\bar{\phi} = -1$ and low temperature values between $T = -3.0$ and $T = -4.43$ (as given at the individual panels). Furthermore, $v_0 = 1$, $\rho_r = 3$, $\zeta = 1$ and $L_x = L_y = 100$. After a short transient, the movie shows a selection of quite intricate regular dynamic behavior of crystallites. In Fig. 5 of the main text the modes of motion are indicated by arrows. The dynamic modes include (a) an elongated hexagonal crystallite with facets of different lengths that swings like a torsion pendulum, i.e., that shows time-periodic chirality, (b) a swinging predominantly striped localized state that also periodically adapts its shape, (c) a wobbling state with a crystalline core of nearly bow-tie shape embedded into stripe domains (the dynamics seems to show several frequencies). Then, panels (d) to (g) show other moving stripe-hexagon two-phase localized states with star-, and hexagon-shaped crystalline cores and outer stripe regions of different degrees of asymmetry. The state in panel (e) seems to wave, while (f) simply rotates, and (g) wobbles and very slowly rotates. Finally, panel (h) shows a dominantly stripe state with a few individual peaks at some stripe ends. After a long transient a rigid-body rotation emerges.

B. Microscopic derivation of amended active PFC model

Here, we present a microscopic derivation of the PFC model given by Eqs. (1) and (2) in the main text. While the general phenomenology described by our model can be found in a variety of systems, we here focus for specificity on one of the most widely used particle-based active matter models – the active Brownian particle (ABP) [9], corresponding to overdamped spherical self-propelling particles. It is well known that ABPs exhibit both motility-induced phase separation (MIPS) [10] and crystalline phases [11]. More recently, it has been found in particle-based simulations that the velocity field of ABPs in a MIPS cluster forms vortex-like structures [12], this is a form of spontaneous collective rotation quite similar to the one that our field-theoretical model predicts. Also, systems of Quincke rollers, which are in many respects similar to the ABPs considered here (for instance in the absence of intrinsic chirality), as they have experimentally been found to form freestanding rotating particle clusters [13].

The microscopic equations of motion for an ABP are given by

$$\dot{\mathbf{r}}_i(t) = v_0\hat{\mathbf{u}}(\varphi_i(t)) - \beta D_\mathrm{T}\nabla_{\mathbf{r}_i}U(\{\mathbf{r}_j\}) + \sqrt{2D_\mathrm{T}}\boldsymbol{\Lambda}_{\mathrm{T},i}(t), \tag{8}$$

$$\dot{\varphi}_i(t) = \sqrt{2D_\mathrm{R}}\Lambda_{\mathrm{R},i}(t) \tag{9}$$

with positions $\mathbf{r}_i = (x_{1,i}, x_{2,i})^\mathrm{T}$ and orientation φ_i of the i-th particle, orientation vector $\hat{\mathbf{u}}_i = (\cos(\varphi_i), \sin(\varphi_i))^\mathrm{T}$, translational and rotational diffusion coefficients D_T and D_R, thermodynamic beta β, potential U, and zero-mean Gaussian white noises $\boldsymbol{\Lambda}_{\mathrm{T},i}$ and $\Lambda_{\mathrm{R},i}$. The Langevin equations (8) and (9) are stochastically equivalent to the Smoluchowski equation

$$\begin{aligned}\dot{\mathfrak{P}}(\{\mathbf{r}_j,\varphi_j\},t) = &\sum_{i=1}^{N}\big(D_\mathrm{T}\nabla^2_{\mathbf{r}_i} + D_\mathrm{R}\partial^2_{\varphi_i} - v_0\hat{\mathbf{u}}(\varphi_i)\cdot\nabla_{\mathbf{r}_i}\big)\mathfrak{P}(\{\mathbf{r}_j,\varphi_j\},t)\\ &+ D_\mathrm{T}\beta\nabla_{\mathbf{r}_i}\cdot\big(\mathfrak{P}(\{\mathbf{r}_j,\varphi_j\},t)\nabla_{\mathbf{r}_i}U(\{\mathbf{r}_j\})\big)\end{aligned} \tag{10}$$

with the N-body distribution $\mathfrak{P}$. We moreover define the orientation-dependent n-particle density

$$\varrho^{(n)}(\mathbf{r},\dots,\mathbf{r}_n,\varphi,\dots,\varphi_n,t) = \frac{N!}{(N-n)!}\Bigg(\prod_{i=n+1}^{N}\int_{\mathbb{R}^2}\mathrm{d}^2r_i\int_0^{2\pi}\mathrm{d}\varphi_i\Bigg)\mathfrak{P}(\{\mathbf{r}_j\},t) \tag{11}$$

and the orientation-dependent pair distribution function

$$g(\mathbf{r}_1,\mathbf{r}_2,\varphi_1,\varphi_2)=\frac{\varrho^{(2)}(\mathbf{r}_1,\mathbf{r}_2,\varphi_1,\varphi_2)}{\varrho(\mathbf{r}_1,\varphi_1)\varrho(\mathbf{r}_2,\varphi_2)}\,. \tag{12}$$

If we integrate Eq. (10) over the coordinates of all particles except for one, we get the exact dynamic equation for the one-particle density

$$\dot{\varrho}^{(1)}(\mathbf{r}_1,\varphi_1,t)=\Big(D_\mathrm{T}\nabla^2_{\mathbf{r}_1}+D_\mathrm{R}\partial^2_{\varphi_1}-v_0\hat{\mathbf{u}}(\varphi_1)\cdot\nabla_{\mathbf{r}_1}\Big)\varrho^{(1)}(\mathbf{r}_1,\varphi_1,t)+\mathcal{I}_\mathrm{int}(\mathbf{r}_1,\varphi_1,t) \tag{13}$$

with the interaction term

$$\mathcal{I}_\mathrm{int}(\mathbf{r}_1,\varphi_1,t)=\beta D_\mathrm{T}\nabla_{\mathbf{r}_1}\cdot\int_{\mathbb{R}^2}\mathrm{d}^2r_2\int_0^{2\pi}\mathrm{d}\varphi_2\,\varrho^{(1)}(\mathbf{r}_1,\varphi_1,t)\varrho^{(1)}(\mathbf{r}_2,\varphi_2,t)g(\mathbf{r}_1,\mathbf{r}_2,\varphi_1,\varphi_2)\nabla_{\mathbf{r}_1}U_2(r_{12}), \tag{14}$$

where we have assumed that the two-body interaction potential U_2 depends only on the distance r_{12} between two particles. In other words, we assume that the particles are spherical, and that there is no external potential (which could, however, be easily added). The difficulty is that Eq. (14) depends on the unknown function g, which needs to be obtained from a suitable closure relation. In the derivation of PFC models this closure is usually obtained using equilibrium theorems from classical density functional theory [14], however, this is not sufficient for describing the formation of MIPS clusters [15].

Exploiting translational and rotational invariance and assuming temporal homogeneity, we can write g as $g(r,\theta_1,\theta_2)$ [16] with the angles

$$\theta_1=\varphi_\mathrm{R}-\varphi_1, \tag{15}$$
$$\theta_2=\varphi_2-\varphi_1 \tag{16}$$

and the distance vector

$$\mathbf{r}_2-\mathbf{r}_1=r\hat{\mathbf{u}}(\varphi_\mathrm{R}). \tag{17}$$

Moreover, we perform a Fourier expansion of g. From previous work [8, 16, 17], it is known that considering the dependence on θ_1 is sufficient to reproduce the effect that is of interest here, namely the existence of an effective density-dependent swimming speed (see Ref. [18] for a derivation taking both angles into consideration). Therefore, we restrict ourselves to the simple expansion

$$g(r,\theta_1,\theta_2)\approx g_0(r)+g_1(r)\cos(\theta_1) \tag{18}$$

with the lowest-order Fourier modes g_0 and g_1. Note that, due to the symmetry of the problem, there is no contribution proportional to $\sin(\theta_1)$. Using Eq. (18), Eq. (14) takes the form

$$\mathcal{I}_\mathrm{int}(\mathbf{r}_1,\varphi_1,t)=\mathcal{I}_\mathrm{ad}(\mathbf{r}_1,\varphi_1,t)+\mathcal{I}_\mathrm{sup}(\mathbf{r}_1,\varphi_1,t) \tag{19}$$

with the adiabatic interaction term

$$\mathcal{I}_\mathrm{ad}(\mathbf{r}_1,\varphi_1,t)=\beta D_\mathrm{T}\nabla_{\mathbf{r}_1}\cdot\int_{\mathbb{R}^2}\mathrm{d}^2r_2\int_0^{2\pi}\mathrm{d}\varphi_2\,\varrho^{(1)}(\mathbf{r}_1,\varphi_1,t)\varrho^{(1)}(\mathbf{r}_2,\varphi_2,t)g_0(r_{12})\nabla_{\mathbf{r}_1}U_2(r_{12}). \tag{20}$$

and the superadiabatic interaction term

$$\mathcal{I}_\mathrm{sup}(\mathbf{r}_1,\varphi_1,t)=\beta D_\mathrm{T}\nabla_{\mathbf{r}_1}\cdot\int_{\mathbb{R}^2}\mathrm{d}^2r_2\int_0^{2\pi}\mathrm{d}\varphi_2\,\varrho^{(1)}(\mathbf{r}_1,\varphi_1,t)\varrho^{(1)}(\mathbf{r}_2,\varphi_2,t)g_1(r_{12})\cos(\theta_1)\nabla_{\mathbf{r}_1}U_2(r_{12}). \tag{21}$$

(The rationale behind this terminology will become clear below.) We also make the Cartesian orientational expansion [19]

$$\varrho^{(1)}(\mathbf{r},\hat{\mathbf{u}},t)\approx\rho(\mathbf{r},t)+\mathbf{P}(\mathbf{r},t)\cdot\hat{\mathbf{u}}, \tag{22}$$

with the density

$$\rho(\mathbf{r},t)=\frac{1}{2\pi}\int_0^{2\pi}\mathrm{d}\varphi\,\varrho^{(1)}(\mathbf{r},\hat{\mathbf{u}},t) \tag{23}$$

and the polarization

$$\rho(\mathbf{r},t) = \frac{1}{\pi}\int_0^{2\pi}\mathrm{d}\varphi\,\varrho^{(1)}(\mathbf{r},\hat{\mathbf{u}},t)\hat{\mathbf{u}}(\varphi). \tag{24}$$

The key idea (and the main novelty of our derivation compared to previous work) is now that we treat $\mathcal{I}_{\mathrm{ad}}$ and $\mathcal{I}_{\mathrm{sup}}$ separately. For $\mathcal{I}_{\mathrm{ad}}$, we first evaluate the integral over φ_2 to find

$$\mathcal{I}_{\mathrm{ad}}(\mathbf{r}_1,t) = 2\pi\beta D_{\mathrm{T}}\nabla_{\mathbf{r}_1}\cdot\left(\varrho^{(1)}(\mathbf{r}_1,\varphi_1,t)\int_{\mathbb{R}^2}\mathrm{d}^2r_2\rho(\mathbf{r}_2,t)g_0(r_{12})\nabla_{\mathbf{r}_1}U_2(r_{12})\right), \tag{25}$$

where we used Eq. (22). Next, we make the adiabatic approximation [20, 21]

$$\int_{\mathbb{R}^2}\mathrm{d}^2r_2\rho(\mathbf{r}_2,t)g_0(r_{12})\nabla_{\mathbf{r}_1}U_2(r_{12}) = \nabla_{\mathbf{r}_1}\frac{\delta\mathcal{F}_{\mathrm{exc}}[\rho]}{\delta\rho(\mathbf{r}_1,t)} \tag{26}$$

with the excess free energy $\mathcal{F}_{\mathrm{exc}}[\rho]$ (which is the difference between the free energy of an interacting and a noninteracting system). Inserting Eq. (26) into Eq. (25) gives

$$\mathcal{I}_{\mathrm{ad}}(\mathbf{r}_1,t) = 2\pi\beta D_{\mathrm{T}}\nabla_{\mathbf{r}_1}\cdot\left(\varrho^{(1)}(\mathbf{r}_1,\varphi_1,t)\nabla_{\mathbf{r}_1}\frac{\delta\mathcal{F}_{\mathrm{exc}}[\rho]}{\delta\rho(\mathbf{r}_1,t)}\right). \tag{27}$$

If we replace $\varrho^{(1)} \approx \rho/(2\pi)$ in Eq. (27), we find

$$\mathcal{I}_{\mathrm{ad}}(\mathbf{r}_1,t) = \beta D_{\mathrm{T}}\nabla_{\mathbf{r}_1}\cdot\left(\rho(\mathbf{r}_1,t)\nabla_{\mathbf{r}_1}\frac{\delta\mathcal{F}_{\mathrm{exc}}[\rho]}{\delta\rho(\mathbf{r}_1)}\right). \tag{28}$$

Now we turn to $\mathcal{I}_{\mathrm{sup}}(\mathbf{r}_1,\varphi_1,t)$, where we will follow the standard framework of the interaction-expansion-method [17, 18] by simply assuming that the function g_1 is known from simulations (which it is for ABPs [22–24]). Moreover, we write

$$\nabla_{\mathbf{r}_1}U_{r_{12}} = -\hat{\mathbf{u}}(\varphi_{\mathrm{R}})U_2'(r_{12}), \tag{29}$$

where the prime indicates a derivative with respect to r_{12}. If we insert Eqs. (22) and (29) into Eq. (21) and perform a gradient expansion [17, 25] truncated at zeroth order, we can evaluate the integrals and find (dropping arguments)

$$\mathcal{I}_{\mathrm{sup}}(\mathbf{r},\varphi,t) = \zeta\hat{\mathbf{u}}\cdot\nabla(\rho(\rho+\hat{\mathbf{u}}\cdot\mathbf{P})) \tag{30}$$

with

$$\zeta = -2\pi^2\beta D_{\mathrm{T}}\int_0^\infty\mathrm{d}r\,rU_2'(r)g_1(r). \tag{31}$$

We now insert Eqs. (19), (22), (28) and (30) into Eq. (13) to find

$$\begin{aligned}\dot{\rho}+\hat{\mathbf{u}}\cdot\dot{\mathbf{P}} = {}& D_{\mathrm{T}}\nabla^2\rho + D_{\mathrm{T}}\nabla^2\hat{\mathbf{u}}\cdot\mathbf{P} - D_{\mathrm{R}}\hat{\mathbf{u}}\cdot\mathbf{P} - v_0\hat{\mathbf{u}}\cdot\nabla(\rho+\hat{\mathbf{u}}\cdot\mathbf{P})\\ &+\beta D_{\mathrm{T}}\nabla\cdot\left(\rho(\mathbf{r}_1,t)\nabla\frac{\delta\mathcal{F}_{\mathrm{exc}}[\rho]}{\delta\rho}\right)+\zeta\hat{\mathbf{u}}\cdot\nabla(\rho(\rho+\hat{\mathbf{u}}\cdot\mathbf{P})).\end{aligned} \tag{32}$$

Next, we observe

$$\nabla^2\rho = \beta\nabla\cdot\left(\rho\nabla\frac{\delta\mathcal{F}_{\mathrm{id}}[\rho]}{\delta\rho}\right) \tag{33}$$

with the ideal gas free energy

$$\mathcal{F}_{\mathrm{id}}[\rho] = \beta^{-1}\int\mathrm{d}^2r\,\rho(\ln(\lambda^3\rho)-1) \tag{34}$$

and the (irrelevant) thermal de Broglie wavelength λ. If we integrate Eq. (32) over φ, we find (using Eq. (33))

$$\dot{\rho} = \beta D_{\mathrm{T}}\nabla\cdot\left(\rho(\mathbf{r},t)\nabla\frac{\delta\mathcal{F}[\rho,\mathbf{P}]}{\delta\rho}\right) - \frac{v_0}{2}\nabla\cdot\mathbf{P} + \frac{\zeta}{2}\nabla(\rho\mathbf{P}) \tag{35}$$

with the total free energy

$$\mathcal{F}[\rho,\mathbf{P}] = \mathcal{F}_{\mathrm{id}}[\rho] + \mathcal{F}_{\mathrm{exc}}[\rho] + \beta^{-1}\int \mathrm{d}^2 r\, \frac{\mathbf{P}^2}{2}. \tag{36}$$

Making a constant mobility approximation [4] for the first term in Eq. (35) and defining the density-dependent swimming speed

$$v(\rho) = v_0 - \zeta\rho, \tag{37}$$

we find

$$\dot{\rho} = \beta D_{\mathrm{T}} \nabla^2 \frac{\delta \mathcal{F}[\rho,\mathbf{P}]}{\delta\rho} - \frac{1}{2}\nabla\cdot(v(\rho)\mathbf{P}). \tag{38}$$

Similarly, we can multiply Eq. (32) by $\hat{\mathbf{u}}$ and then integrate over φ to find

$$\dot{\mathbf{P}} = D_{\mathrm{T}}\beta\nabla^2 \frac{\delta \mathcal{F}[\rho,\mathbf{P}]}{\delta\mathbf{P}} - D_{\mathrm{R}}\beta \frac{\delta \mathcal{F}[\rho,\mathbf{P}]}{\delta\mathbf{P}} - \nabla(v(\rho)\rho), \tag{39}$$

having used Eq. (36). The last step is to perform the rescaling

$$t = \frac{r_0^2}{D_{\mathrm{T}}}\tilde{t}, \tag{40}$$
$$\mathbf{r} = r_0\tilde{\mathbf{r}}, \tag{41}$$
$$\mathcal{F} = \beta^{-1}\tilde{\mathcal{F}}, \tag{42}$$
$$\rho = \rho_0\tilde{\rho}, \tag{43}$$
$$\mathbf{P} = 2\rho_0\tilde{\mathbf{P}}, \tag{44}$$
$$\tilde{D}_{\mathrm{r}} = D_{\mathrm{R}}\frac{r_0^2}{D_{\mathrm{T}}}, \tag{45}$$
$$\tilde{v}_0 = \frac{\rho_0 r_0}{D_{\mathrm{T}}}v_0, \tag{46}$$
$$\tilde{\zeta} = \frac{\rho_0^2 r_0}{D_{\mathrm{T}}}\zeta, \tag{47}$$

where the quantities with a tilde are dimensionless. The parameters ρ_0 and r_0 are undetermined at this stage and can be fixed via the free energy. Specifically, the choice $D_c = 0.2$ in Eq. (4) for the polarization-dependent part of the free energy implies $4\rho_0^2 r_0^2 = 0.2$.

Inserting Eqs. (40)–(47) into Eqs. (38) and (39) and dropping the tildes finally gives

$$\dot{\rho} = \nabla^2 \frac{\delta \mathcal{F}[\rho,\mathbf{P}]}{\delta\rho} - \nabla\cdot(v(\rho)\mathbf{P}), \tag{48}$$
$$\dot{\mathbf{P}} = \nabla^2 \frac{\delta \mathcal{F}[\rho,\mathbf{P}]}{\delta\mathbf{P}} - D_{\mathrm{r}} \frac{\delta \mathcal{F}[\rho,\mathbf{P}]}{\delta\mathbf{P}} - \nabla(\alpha v(\rho)\rho) \tag{49}$$

with $\alpha = 1/2$. Note that the value of α depends primarily on the rescaling choice (44), the value $\alpha = 1$ (which is also common) could have been obtained by setting $\mathbf{P} = \sqrt{2}\rho_0\tilde{\mathbf{P}}$ instead [26].

Finally, it is worth discussing some general physical insights that can be gained from this derivation. First, the usual active PFC model is derived from dynamical density functional theory (DDFT) and thereby inherits one of its key limitations – it is based on the adiabatic approximation [21], where one assumes that the correlations in the system are the same as in an equilibrium system with the same density. The microscopic origin of MIPS, however, is the existence of nonequilibrium correlations [8], such that DDFT and PFC models cannot describe MIPS in their standard form. Our model, however, explicitly incorporates nonequilibrium correlations (resulting in so-called "superadiabatic forces" [15]) via the higher-order Fourier mode g_1. This is why our PFC model is capable of describing MIPS.

A second aspect is the sign of the parameter ζ. Since a microscopic expression (Eq. (31)) is available, the value of ζ can be calculated, and doing this shows for repulsive ABPs that it is positive [17]. Physically, this means that it is more likely to find another particle in front of a tagged particle than to find it behind it [8]. It also implies that, as the density ρ is increased, the density-dependent swimming speed (37) goes down, which is the mechanism typically responsible for MIPS [10]. However, for other microscopic setups negative values of ζ might also be conceivable. For instance, a derivation for ζ was obtained in Eq. (27) of Ref. [27] for a system with non-reciprocal (vision cone) interactions [28]. In this system, the sign of ζ is determined by a balance of short-ranged repulsive and long-ranged attractive vision-cone interactions, and for strong attractive interactions ζ becomes negative. (A PFC model for systems with nonreciprocal interactions that form rotating crystals was developed in Ref. [29].)

Third, the only polarization dependence in the expression (36) for the free energy is a term in $\mathbf{P}$, which is consistent with the choice made in all our simulations. As discussed below, in general the free energy can have terms of higher order in $\mathbf{P}$. This will happen if there are orientation-dependent interactions in the equilibrium limit, in other words, if we consider particles that are not spherical but, e.g., rodlike. Moreover, such a contribution can emerge from nonequilibrium alignment interactions as present, e.g., in the Toner-Tu model [30]. Concerning the ρ-dependent terms, the microscopic result obtained from density functional theory, involving a logarithm in the ideal gas free energy (cf. Eq. (34)) and a convolution integral in the excess free energy is in PFC models usually simplified via a combined Taylor and gradient expansion [21]. The specific form used here was obtained in Ref. [5]. A systematic discussion of possible contributions to $\mathcal{F}$ in an active PFC model and when to find them is provided in Ref. [26].

To obtain Eqs. (5) and (6) (i.e., Eqs. (1) and (2) of the main text) from Eq. (48), one replaces ρ by $\rho_r + \phi$. However, the form in Eq. (48) is useful when comparing the the limiting case of a standard MIPS model as in Ref. [8]. This is done below in section D.

C. Linear stability of uniform state - dispersion relations and spinodals

Next we provide the linear stability analysis of uniform steady states for the higher-order active PFC model in Eqs. (5) and (6) (i.e., Eqs. (1) and (2) of the main text). Introducing the notation $\mathbf{w} = (\phi, P)^{\mathrm{T}}$, the uniform steady states $\mathbf{w}^* = (\bar{\phi}, 0)^{\mathrm{T}}$ solve Eqs. (5) and (6) with $\partial_t \mathbf{w} = \mathbf{0}$ for any $\bar{\phi}$ (due to mass conservation). Linearizing the kinetic equations in small perturbations $\delta\mathbf{w}e^{ikx+\lambda t}$ about $\mathbf{w}^*$ yields the linear eigenvalue problem

$$\lambda \delta\mathbf{w} = \underline{L}\delta\mathbf{w} \tag{50}$$

with the Jacobian matrix

$$\underline{L} = \begin{pmatrix} L_\phi & -ik(v_0 - \zeta\bar{\phi} - \zeta\rho_r) \\ -ik\alpha(v_0 - 2\zeta\bar{\phi} - 2\zeta\rho_r) & L_P \end{pmatrix}. \tag{51}$$

Here,

$$\begin{aligned} L_\phi =& -k^2\Bigg[-\left(C_0(T) + D_0\bar{\phi} + \frac{E_0}{2}\bar{\phi}^2\right) + \left(C_2(T) + \frac{2}{3}D_{11}\bar{\phi}\right)k^2 \\ & - \left(C_4(T) + \frac{1}{12}E_{1122}\bar{\phi}^2\right)k^4 + C_6k^6\Bigg], \qquad (52) \\ L_P =& -(D_ck^2 + D_{nc}). \qquad (53) \end{aligned}$$

represent the stability problem in the completely decoupled passive case. In the active case, the two branches of the dispersion relation $\lambda(k)$ are given by

$$\lambda_\pm = \frac{1}{2}\left[L_\phi + L_P \pm \sqrt{(L_\phi + L_P)^2 - 4\det\underline{L}}\right], \tag{54}$$

where

$$\det\underline{L} = L_\phi L_P + k^2\alpha[v_0^2 + 2\zeta^2(\bar{\phi} + \rho_r)^2 - 3v_0\zeta(\bar{\phi} + \rho_r)] \tag{55}$$

is the determinant of the Jacobian (51). The resulting $\mathrm{Re}(\lambda)$ and $\mathrm{Im}(\lambda)$ correspond to growth/decay rates and frequencies, respectively, of harmonic modes in dependence of the wavenumber k. The λ are real for $(L_\phi + L_P)^2 \geq 4\det\underline{L}$. Then, v_0^2 and $2\zeta^2(\bar{\phi} + \rho_r)^2$ always act stabilizing with increasing $|v_0|$ and $|\zeta|$, as the larger eigenvalue (λ_+) decreases. Only the term $3v_0\zeta(\bar{\phi} + \rho_r)$ acts destabilizing for $v_0, \zeta > 0$.

All borders of linear stability (spinodals) are given by $\det\underline{L} = 0$. As phase separation is a large-scale instability the corresponding onset always occurs at $k = 0$. Therefore, to obtain the corresponding spinodals we simplify Eq. (55) for $k \ll 1$, leading to the condition

$$T = -\frac{C_0^*}{C_0'} - \frac{D_0}{C_0'}\bar{\phi} - \frac{E_0}{2C_0'}\bar{\phi}^2 + \frac{\alpha}{C_0' D_{nc}}[v_0^2 - 3v_0\zeta(\rho_r + \bar{\phi}) + 2\zeta^2(\rho_r + \bar{\phi})^2]. \tag{56}$$

where $C_0 = C_0^* + C_0' T$. The spinodal's maximum T_c is at

$$\bar{\phi}_c = \frac{\alpha(3v_0\zeta - 4\zeta^2\rho_r) + D_0 D_{nc}}{4\alpha\zeta^2 - E_0 D_{nc}}\,. \tag{57}$$

The coordinates of the critical point (ϕ_c,T_c) indicate how v_0 and ζ impact phase separation. An analysis of $\partial_\zeta T(\phi_c) = 0$ shows that the trace of the critical point in the $(\bar{\phi}, T)$-plane when ζ is changed can itself have a maximum and a minimum, namely,

$$\zeta_{\max} = \frac{D_{nc}(E_0\rho_r - D_0)}{3\alpha v_0}, \quad \text{i.e., when } \phi_c = -\rho_r \quad (\rho_c = 0) \tag{58}$$

$$\zeta_{\min} = -\frac{3v_0 E_0}{4(E_0\rho_r - D_0)}, \quad \text{i.e., at } \phi_c = -\frac{D_0}{E_0} \tag{59}$$

This indicates that there exist distinct parameter regions where ζ suppresses or enhances phase separation. Specifically, $D_0 \geq 0$ allows ζ to raise the border of linear stability, though other parameters have to be adapted to avoid that the region of phase separation is "swallowed up" by the region of pattern formation. Here, this is accomplished by setting a large value for C_6. For the case shown in Fig. 2 (d) of the main text we use $D_0 = 0$ and $C_6 = 200$ (see Table I). Such a differentiated influence of ζ well agrees with literature results for standard MIPS models as further discussed in section D.

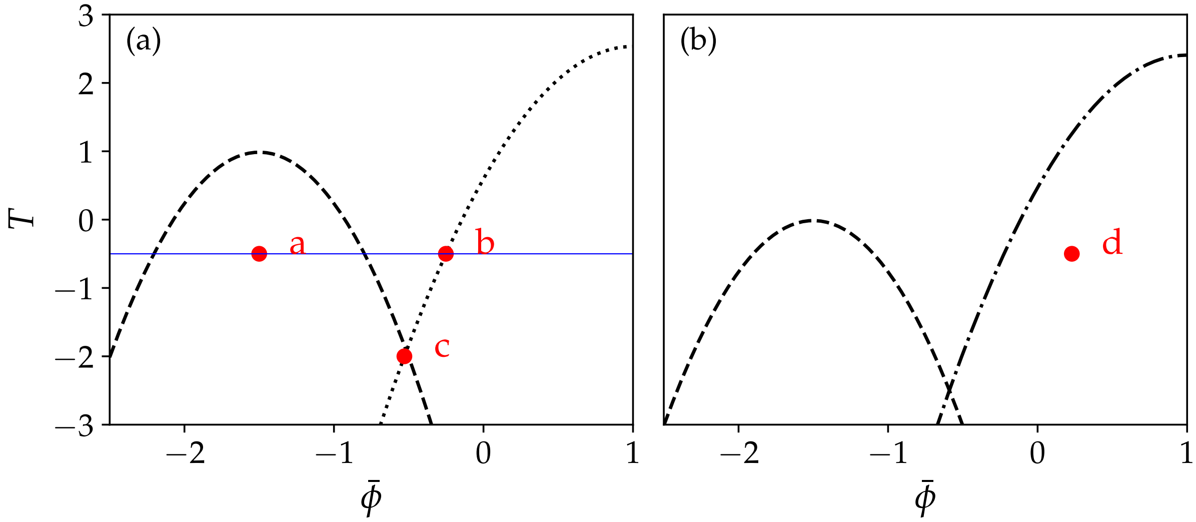

FIG. 1. Spinodals of the extended PFC model Eqs. (5) and (6) in the $(\bar{\phi}, T)$-plane. Black dashed, dotted, and dash-dotted lines give the spinodals, i.e., the stability thresholds of uniform states with respect to a large-scale stationary (Cahn-Hilliard), small-scale stationary (conserved-Turing), and small-scale oscillatory (conserved-wave) instability, respectively. The parameters for panels (a) and (b) are identical to the respective parameters for Fig. 2 (a) and (b) of the main text. In particular, (a) represents the passive limit and (b) has activity parameters $v_0 = 1$, $\zeta = 0$. In both panels there exists a codimension-2 point where the onset of large- and small-scale instability coincide, i.e., the spinodals cross. The red dots mark the positions of dispersion relations given in Fig. 2 and the blue line indicates the parameter choices for Fig. 4.

The stability thresholds of the uniform state in the $(\bar{\phi}, T)$-plane for the parameters of Ref. [5] are shown in Fig. 1 for an extended range as compared to Fig. 2 (a) and (b) of the main text. The same passive and active cases are shown. In each case, at intermediate $\bar{\phi}$ liquid-gas phase separation occurs (resulting from a large-scale stationary instability with a conservation law, i.e., a Cahn-Hilliard instability), if the temperature is lower than a critical value T_c. At large densities, crystallization occurs due to a small-scale stationary instability with a conservation law, i.e., a conserved-Turing instability in the passive case or due to a small-scale stationary (again conserved-Turing) or small-scale oscillatory (i.e., conserved-wave) instability in the active case. For more information on the employed classification of instabilities, see SM of [31] and introduction of [32]. Large- and small-scale instabilities occur simultaneously at the codimension-2 point at $(\bar{\phi}, T) \approx (-0.5, -2)$. The critical point for phase separation is at $(\bar{\phi}, T) \approx (-1.5, 1)$ in the passive case. The spinodal line and critical point for phase separation are strongly influenced by density-independent and density-dependent velocity. Increasing the former suppresses phase separation by shifting

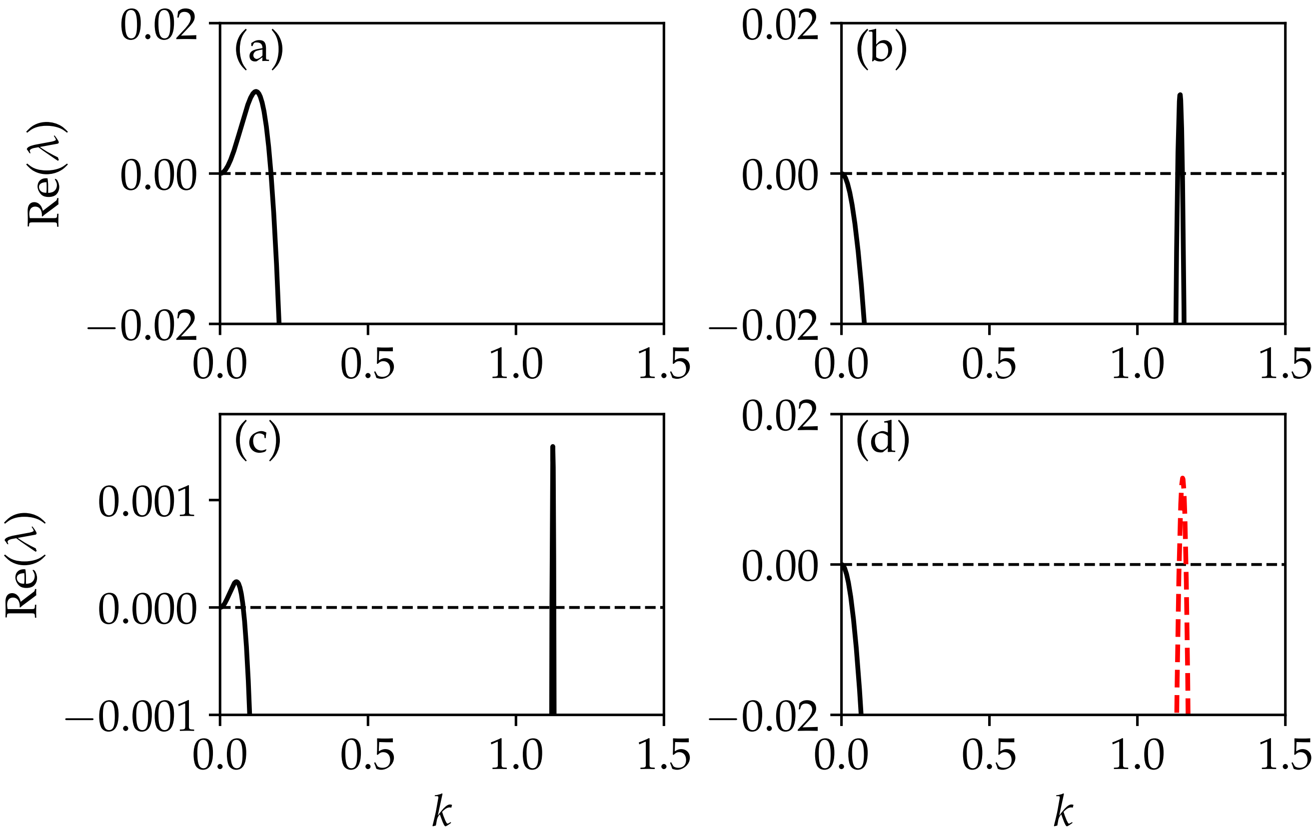

FIG. 2. Dispersion relations of the extended PFC model in Eqs. (5) and (6). Black solid [red dashed] lines indicate real [complex] eigenvalues. The dispersion relations presented in (a) at $\bar{\phi} = -1.5$, $T = -0.5$, and $v_0 = 0$, (b) at $\bar{\phi} = -0.2515$, $T = -0.5$, and $v_0 = 0$, and (c) at $\bar{\phi} = -0.52895$, $T = -2.$, and $v_0 = 0$ all show stationary instabilities. The dispersion relation in (a) corresponds to a Cahn-Hilliard instability, the one in (b) corresponds to a conserved-Turing instability. Panel (c) presents a case close to the codimension-2 point, i.e., the point where Cahn-Hilliard and conserved-Turing instabilities occur simultaneously. Note that in panel (c) the scale of the y-axis is much smaller than in the other panels. Panel (d) shows an active case at $\bar{\phi} = 0.229$, $T = -0.5$, and $v_0 = 1$, $\zeta = 0$. The dispersion relation corresponds to a conserved-wave instability. The remaining parameters are given in Table I.

the critical point and the entire spinodal to lower temperatures while the latter may enhance or further suppress phase separation. However, the linear stability threshold for crystallization barely moves in the investigated parameter range. Nevertheless, the coexistence regions outside the spinodals as obtained by nonlinear considerations (see below) show more pronounced changes, see Fig. 2 of the main text and Fig. 7 in the present SM. There, density-independent and density-dependent velocity similarily suppress and enhance/suppress crystallization, respectively, indicating that the latter represents motility-induced crystallization (MIC).

Phase diagrams with a similar appearence of regions where solid, liquid and gas occur, are obtained in Refs. [33, 34] from particle-based simulations of hard sphere systems. Their different choice of nondimensionalization results in a different set of control parameters and different pathways through physical parameter space. For instance, the Peclet number in [33] is at fixed remaining parameters inversely proportional to temperature. This implies that inverting the y-axis of their Fig. 1a one would expect to obtain a diagram similar to Fig. 2 of the main text or (zoomed out) as Fig. 1 and Fig. 7 of this SM. This is indeed the case.

Examples of corresponding dispersion relations are presented in Fig. 2. There, black solid and red dashed lines correspond to the real and complex eigenvalues, respectively. While in Fig. 2 (a)-(c) dispersion relations in the passive limit are presented, the dispersion relation in Fig. 2 (d) is at $v_0 = 1$. In Fig. 2 (a) at $T = -0.5$, and $\bar{\phi} = -0.5$ the shown dispersion relation is at parameters well above the onset of a Cahn-Hilliard instability. At the onset of instability, $k = 0$ is the mode with the largest growth rate. Above the onset, the eigenvalue at $k = 0$ remains zero and there is an adjacent band of unstable wavenumbers. In time simulations, this gives rise to large-scale structures, i.e., a phase-separated state. This instability is similar to the one found for the Cahn-Hilliard equation. At the same temperature $T = -0.5$, but at a higher mean density $\phi = -0.2515$ the dispersion relation is at parameters slightly above the onset of a conserved-Turing instability. A small band of wave numbers close to $k \approx 1.1444$ is unstable. Directly at onset a time simulation is expected to result in a spatially periodic state, i.e., a crystal of corresponding structure length. Further above onset the periodicity of the crystal slightly deviates from the linear result.

At a codimension-2 point the Cahn-Hilliard and the conserved-Turing instability are both at their threshold. A typical dispersion relation close to this point, where both instabilities occur simultaneously, is presented in Fig. 2 (c) at $T = -2$ and $\bar{\phi} = -0.52895$. There, two bands of unstable wave numbers exist, one adjacent to $k = 0$ and another one around $k_c \approx 1.1533$. In a time simulation these two instabilities compete. The nonlinear state that is eventually realized can, however, not be predicted from the linear analysis. Nevertheless, the existence of the codimension-2 point is a first indicator for the existence of three-phase (vapor-liquid-solid) coexistence. Finally, in Fig. 2 (d) we present a dispersion relation for the active case. As in Fig. 2 (b), a small-scale instability occurs, however, here with complex eigenvalues, i.e., the instability is oscillatory and corresponds to a conserved-wave instability. A time simulation produces a traveling periodic state, i.e., a traveling crystal.

D. Quantitative relation to classical MIPS and active Cahn-Hilliard models

Models solely focusing on motility-induced phase separation (MIPS) have been extensively studied. Notably, the model in Eqs. (16) and (18) of Ref. [8] corresponds to our Eqs. (5) and (6) with the very simple energy functional

$$\mathcal{F}[\rho, p] = \frac{1}{2}\int dx(\rho^2 + \mathbf{p}^2) \tag{60}$$

that in the passive limit allows for no phase transition at all. In contrast, our $\mathcal{F}[\phi, p]$ [Eq. (1)] contains higher-order terms and uses a shifted density ϕ similar to a Cahn-Hilliard (CH) model. Considering a simple standard CH model, the critical density ρ_c determines the position of the double-well potential, i.e., replacing $\phi = \rho - \rho_c$ the CH energy reads

$$\mathcal{F}_{CH}[\rho, \mathbf{p}] = \int dx \left(\frac{(\rho-\rho_c)^2}{2}T + s_2\frac{(\rho-\rho_c)^3}{3} + s_3\frac{(\rho-\rho_c)^4}{4} + \frac{\mathbf{p}^2}{2} \right). \tag{61}$$

where we kept the polarization-dependence as in Eq. (60). Introducing, for convenience, $\rho_{rc} = \rho_r - \rho_c$, where ρ_r is the reference density introduced in section A, an active CH model can be written as

$$\begin{aligned}
\partial_t\phi =& -\nabla(v(\phi)\mathbf{p}) \\
&+ D\Delta\left[T(\phi+\rho_{rc}) + s_2(\phi+\rho_{rc})^2 + s_3(\phi+\rho_{rc})^3\right] && (62)\\
\partial_t\mathbf{P} =& D_c\Delta\mathbf{P} - D_{nc}\mathbf{P} - \nabla\cdot[\alpha v(\phi)\,(\phi+\rho_r)], && (63)\\
\text{with}\qquad v(\phi) =& v_0 - \rho_r\zeta - \phi\zeta\,.
\end{aligned}$$

Note that such a model for $\zeta = 0$ is introduced and briefly studied in chapter 7.2 of [35].

Linearization gives the Jacobian

$$\underline{L} = \begin{bmatrix} -Dk^2(T + 2s_2(\bar{\phi}+\rho_{rc}) + 3s_3(\bar{\phi}+\rho_{rc})^2) & -ik(v_0 - \rho_r\zeta - \bar{\phi}\zeta) \\ -ik\alpha(v_0 - 2\rho_r\zeta - 2\bar{\phi}\zeta) & -D_{nc} - D_c k^2\,, \end{bmatrix} \tag{64}$$

leading to the spinodal for phase separation

$$\begin{aligned}
T =& -2s_2(\bar{\phi}+\rho_{rc}) - 3s_3(\bar{\phi}+\rho_{rc})^2 \\
&- \frac{\alpha}{DD_{nc}}[v_0^2 - 3v_0\zeta(\rho_r+\bar{\phi}) + 2\zeta^2(\rho_r+\bar{\phi})^2].
\end{aligned} \tag{65}$$

In the limit corresponding to the simple energy (60), i.e., for $\rho_r = \rho_c = s_2 = s_3 = 0$ and $T = 1$ we recover the spinodal of Ref. [8], where

$$\zeta(\rho_r + \bar{\phi}) = 3/4v_0 \pm \sqrt{(v_0/4)^2 - DD_{nc}/2\alpha}\,. \tag{66}$$

When displayed in a similar form, the full Eq. (65) writes

$$\begin{aligned}
\zeta(\rho_r+\bar{\phi}) &= \frac{3}{4}v_0 \pm \sqrt{\left(\frac{v_0}{4}\right)^2 - x} \\
\text{with}\qquad x &= \frac{DD_{nc}}{2\alpha}\left(T + 2s_2(\bar{\phi}+\rho_{rc}) + 3s_3(\bar{\phi}+\rho_{rc})^2\right).
\end{aligned} \tag{67}$$

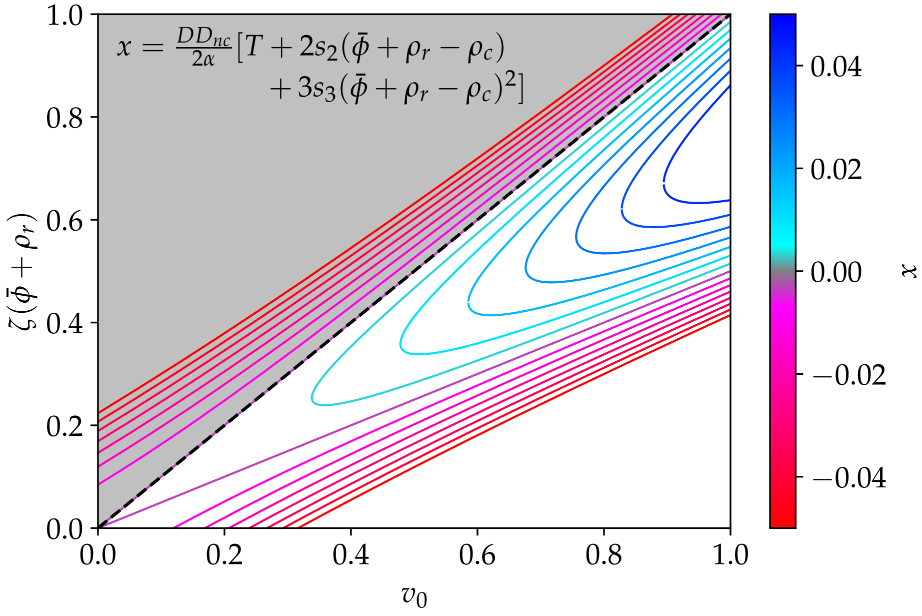

FIG. 3. Spinodals of phase separation in the $(v_0, \zeta(\bar{\phi} + \rho_r))$-plane, given by Eq. (67) for the reduced model (Eqs. (62) and (63)) corresponding to an active Cahn-Hilliard model that itself contains the simple MIPS model in Eqs. (16) and (18) of [8] as special case. Here, x is a compound parameter as given in the legend and defined in (67). Values of x for the various spinodals are given as colorbar. Values above the dashed black line, where $\zeta(\bar{\phi} + \rho_r) > v_0$ are unphysical (shaded gray). For a discusion see accompanying text.

A number of resulting spinodals for different values of x is given in Fig. 3 in the plane spanned by v_0 and $\zeta(\bar{\phi} + \rho_r)$. The plane is bisected by the dashed black line, where $\zeta(\bar{\phi} + \rho_r) = v_0$. Everything above this line is unphysical because there the total activity v becomes negative (shaded gray area). For $x < 0$ (the red lines) this is the case for the upper branch of the spinodal. In consequence, depending on the value of v_0, for $x < 0$ raising ζ from zero will enhance phase separation (at small $v_0 < \sqrt{-2x}$) or eventually cause phase separation (for $v_0 > \sqrt{-2x}$). For $x > 0$ (the blue lines) increasing ζ from zero may first cause phase separation if v_0 is sufficiently large ($v_0 \geq 4\sqrt{x}$). However, a further increase of ζ will eventually suppress phase separation again. Setting $s_2 = s_3 = 0$ and $T = 1$, i.e., using the simple energy (60), this exactly corresponds to the situation shown in Fig. 1 (b) of [8].

Next the spinodal of phase separation of the reduced model, the active CH model (Eqs. (62) and (63)), is compared to the extended active PFC model (Eqs. (5) and (6)) to see how the three discussed models are quantitatively related. In particular, we match the spinodal conditions (Eqs. (65) and (56)) term by term. As the final terms are nearly identical the corresponding condition is simply $D = -C_0'$. The terms quadratic in ϕ give

$$s_3 = \frac{E_0}{6C_0'} \tag{68}$$

while the linear ones give

$$s_2 = \frac{D_0 - E_0\rho_{rc}}{2C_0'}\,. \tag{69}$$

Finally, the constant terms give $2s_2\rho_{rc} + 3s_3\rho_{rc}^2 = \frac{C_0^*}{C_0'}$, leading to

$$\rho_{rc} = \frac{D_0}{E_0} \pm \sqrt{\frac{D_0^2}{E_0^2} - 2\frac{C_0^*}{E_0}} \quad \text{and} \quad s_2 = \mp\frac{E_0}{2C_0'}\sqrt{\frac{D_0^2}{E_0^2} - 2\frac{C_0^*}{E_0}}\,. \tag{70}$$

For the values given in the first row of Table I, we obtain $D = 1$, $s_2 \approx \mp 1.72$ (for $\rho_{rc} \approx 2.07$ and ≈ 0.93 respectively) and $s_3 = 1$. These considerations now allow one to seamlessly discuss the active Cahn-Hilliard model of [35] and the even simpler MIPS model in Eqs. (16) and (18) of [8] as limiting cases of our Eqs. (5) and (6) (i.e., Eqs. (1) and (2) of the main text). Together with the considerations regarding the translation of parameters and fields between the different models the spinodals for phase separation in Fig. 3 are directly valid for the higher-order active PFC model detailed in section A.

E. Numerical methods and set-ups

Time simulations are used to determine phase diagrams and example profiles of steady and dynamic states (Figs. 1-5 of main text) and determine the features of the rotating crystallites. To that end a pseudo-spectral semi-implicit Euler method is employed [36].

The solution measure used for the phase diagrams in Fig. 2 of the main text is the solution type, which is obtained by visual inspection. Solution measures for the rotating crystallites (Fig. 4 of the main text) are their radius and their angular velocity. The former is obtained as a time average by taking a horizontal slice at $y = 0$ and then measuring at which point $\phi(x, 0)$ first reaches a threshold value A, starting from the outer edge and moving in. The threshold value is defined as $A = (\phi_h - \phi_b)p$, i.e., the difference of the highest peak density ϕ_h and the background density ϕ_b is multiplied by a percentage p. For odd localized states we use $p = 0.75$. For even localized states we use $p = 0.65$ as the lack of a central peak results in a lower value of ϕ_h when averaging over time. The time average of the x-value where A is passed gives the cluster radius R. The angular velocity is given in radians per time step. All simulations are performed on a quadratic domain with $L_x = L_y = 100$ and a discretization of $N_x = N_y = 256$ at parameters given in Table I.

The simulations for the phase diagram in the passive case (Fig. 2 (a) of the main text) are initialized with a circular patch of radius $R_I = 25$ and density $\phi(\mathbf{r}) - \bar{\phi} = 2$ on a random background, which is then shifted to match $\bar{\phi}$. All simulations for the phase diagram in the active case are initialized with the counterpart states in the passive limit. This corresponds to first letting the system evolve towards thermodynamic equilibrium and subsequently taking it permanently out of equilibrium by introducing activity. Initial condition for all rotating crystallite states in Figs. 4 and 5 of the main text are rotating crystallite states from previous simulations at neighboring parameter values.

To create bifurcation diagrams, numerical path continuation [37] is used for a one-dimensional domain. To that end the `Matlab` package `pde2path` [38] is used. On the one hand, we follow individual states in parameter space and obtain the branches of uniform, periodic and localized states in Figs. 4 to 6. On the other hand, we follow saddle-node bifurcations using two-parameter continuation to obtain the ranges of existence summarized in Fig. 7.

Solution measures for the bifurcation diagrams are the mean grand potential $\bar{\omega}$, the chemical potential μ, the mean concentration $\bar{\phi}$, the relative mean free energy density $\bar{f} = \bar{f}_{\mathrm{PFC}} - f_0$, where f_0 is f_{PFC} for $\phi = \bar{\phi}$ and the L_2-norm

$$\|\delta \mathbf{u}\| = \sqrt{\frac{1}{L}\int_{-L/2}^{L/2} (\phi - \bar{\phi})^2 + P^2 \,\mathrm{d}x}, \tag{71}$$

where L is the domain size.

Note that bifurcation diagrams that show μ over $\bar{\phi}$ are appropriate for a conserved dynamics (i.e., $\bar{\phi}$ is controlled) and indicate corresponding stability w.r.t. mass-conserving perturbations. If, in contrast the same branches of states are shown in a bifurcation diagram that is plotted over μ the diagram is appropriate for a nonconserved dynamics (i.e., μ is controlled) and indicates corresponding stability w.r.t. perturbations at fixed μ (that normally change mass). See conclusion of [39], sections 3.2 and 3.3 of [37], and the final part of section 2 of [40] for corresponding discussions. Also consider Figs. 4, 6, 9, and 11 of [41] for corresponding 'turnable' plots in the cases of passive phase separation in 1d and 2d, and crystallization in 1d and 2d, respectively.

F. Bifurcation behavior for one-dimensional states

To gain a deeper understanding of the nonlinear system behavior for the parameter set of Ref. [5], we finally present selected bifurcation diagrams of steady states. In particular we focus on the various coexistence regions present in the phase diagram in Fig. 2 of the main text. For relative simplicity and clarity, we limit our attention to one-dimensional systems of a moderate domain size ($L = 100$).

First, we consider the dependence on $\bar{\phi}$ in the passive case at $T = -0.5$, i.e., we analyze a horizontal cut through the phase diagram in Fig. 2 (a) of the main text marked by a horizontal blue line in Fig. 1 of the SM. To obtain steady states we solve Eq. (7) and employ continuation techniques (see section E of SM) to follow branches of uniform and nonuniform states in parameter space. The nonuniform states correspond to liquid-gas, solid-gas and solid-liquid coexistence as well as domain-filling crystals. The bifurcation diagram is presented in Fig. 4 in terms of the L_2-norm Eq. (71), in Fig. 5 in terms of the mean free energy $\bar{f}$, and in Fig. 6 (a) in terms of the chemical potential μ. To identify coexisting states (see below), Fig. 6 (b) gives all branches in the plane spanned by grand potential density (negative of pressure) $\bar{\omega}$ and μ.

First, we inspect Fig. 4: The state of zero norm exists at all $\bar{\phi}$ and corresponds to a uniform gas (at low $\bar{\phi}$) or liquid (at larger $\bar{\phi}$), two states that may coexist (crossing of the black solid line with itself in Fig. 6 (b) at $(\mu, \omega) \approx (1.675, -0.15)$). At low $\bar{\phi}$ the uniform state is the only, therefore globally stable state. Increasing $\bar{\phi}$,

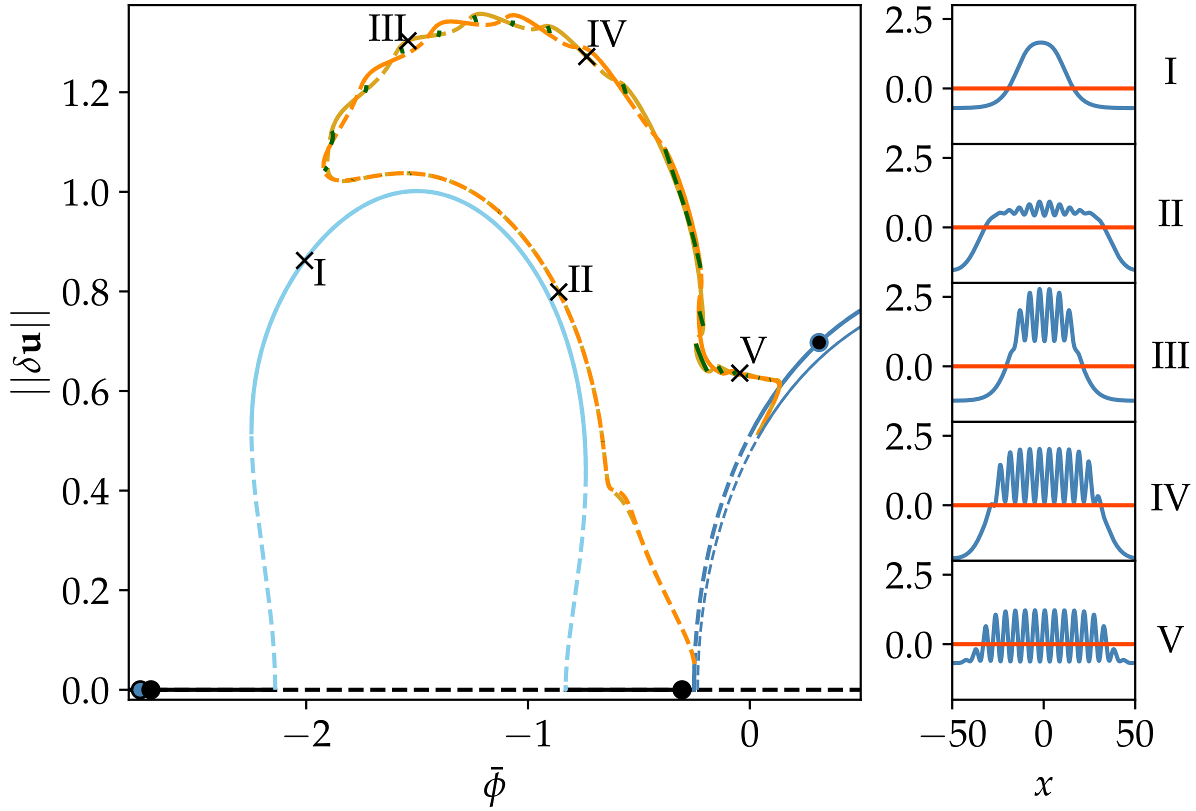

FIG. 4. Bifurcation diagram for the passive case ($v_0 = 0$, $\zeta = 0$) at fixed $T = -0.5$ showing branches of steady states characterized by their L$_2$ norm $\|\delta\mathbf{u}\|$ as a function of the mean density $\bar{\phi}$ for a one-dimensional domain of size $L = 100$. Solid [dashed] lines indicate linearly stable [unstable] states. The black branch represents homogeneous (gas and liquid) states while the light blue line consists of states of liquid-gas coexistence (phase-separated states). The thick [thin] dark blue line corresponds to domain-filling crystalline (periodic) states with $n = 18$ [$n = 19$] peaks. The intertwined dark and light orange lines represent the slanted snaking of branches of localized states with odd and even peak number, respectively. They both represent crystal-gas coexistence and are interconnected by branches of asymmetric states (short dark green lines). The four filled circles indicate two pairs of binodal points, where the fill-color corresponds to the color of the branch the state coexists with, e.g., the state marked by the dark blue-filled circle on the black branch of homogeneous states coexists with the crystal state at the black-filled circle on the dark blue branch. Crosses indicate the loci of states I to V whose density profiles $\phi(x)$ are given in the small panels one the right. Corresponding free energy densities, grand potential densities and chemical potentials are presented in Fig. 5, Fig. 6 (a) and Fig. 6 (b), respectively. The remaining parameters are as in Table I.

eventually it becomes unstable in a subcritical pitchfork bifurcation at $\bar{\phi} \approx -2.140$. It again gains stability at another such bifurcation at $\bar{\phi} \approx -0.830$ before it destabilizes again at a supercritical pitchfork bifurcation at $\bar{\phi} \approx -0.251$. The two leftmost bifurcations are connected by a branch of phase-separated states (blue line) that corresponds (where it is stable) to liquid-gas coexistence, a behavior well known from the Cahn-Hilliard model (see, e.g.,[41]). As the branch emerges subcritically at both ends, the states are initially unstable and gain stability at saddle-node bifurcations at $\bar{\phi} \approx -2.247$ and $\bar{\phi} \approx -0.739$, respectively. Along the part between the two saddle-node bifurcations the phase-separated state is linearly stable, for an example profile see panel I of Fig. 4. The corresponding dependencies of the energy on $\bar{\phi}$ in Fig. 5 show that the phase-separated state represents the global energy minimum shortly after passing the left saddle-node bifurcation (above $\bar{\phi} \approx -2.218$) till $\bar{\phi} \approx -1.829$ shortly before reaching the state of maximal norm. The latter aspect differs from a simple CH model as, here, beyond this point the global minimum is related to gas/liquid-crystal coexistence (see below). The unstable part of the branch consists of nucleation solutions, i.e., threshold states that have to be overcome for transitions between uniform and phase-separated state, i.e., between metastable and stable state, in the binodal region outside the spinodal.

The Maxwell points of coexistence in the thermodynamic limit are obtained using the continuation procedure described in Ref. [42]. For liquid-gas coexistence they are indicated in Fig. 4 by the filled black circles on the branch of uniform states. In Fig. 6 (a) the Maxwell line connecting the two points lies on the upper thin dotted horizontal line (at $\mu \approx 1.854$). This line represents the thermodynamic limit and is approached by the central part of the blue

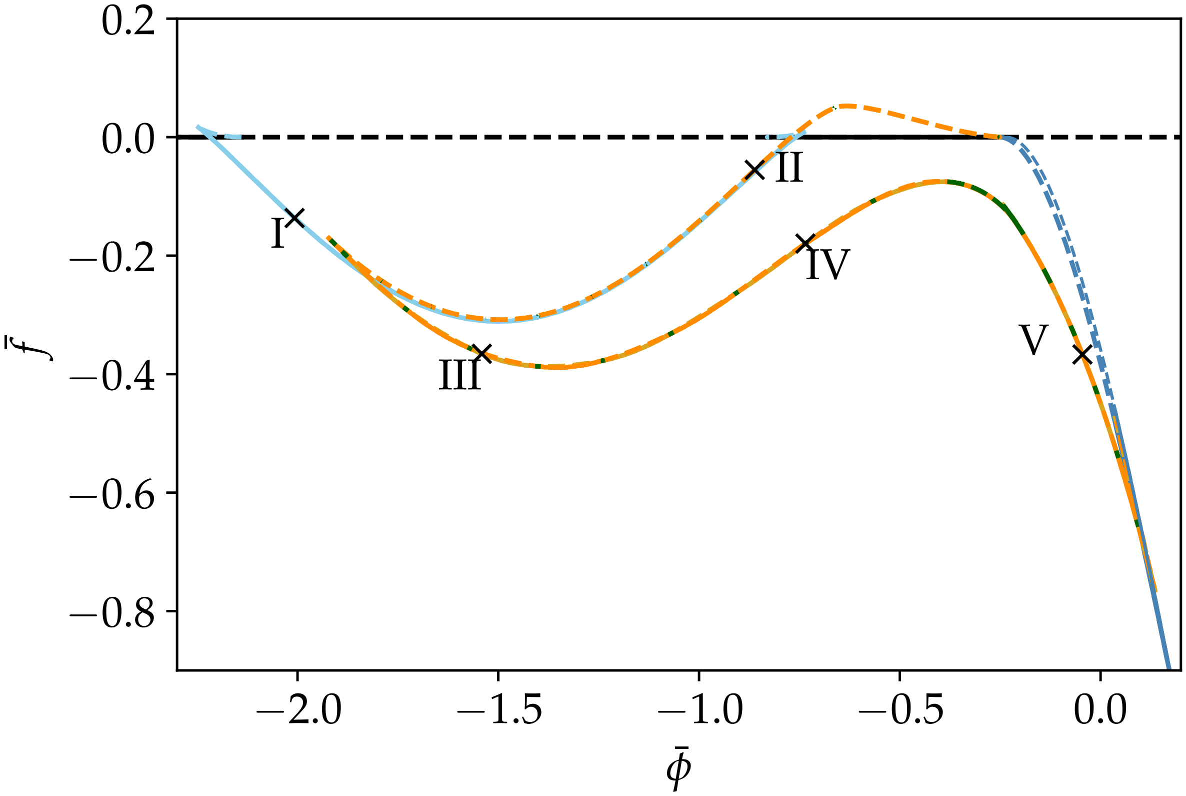

FIG. 5. Shown is the relative mean free energy density $\bar{f}$ as a function of the mean density $\bar{\phi}$ for the passive case analyzed in Fig. 4. All parameters, line styles and symbols are as in Fig. 4.

branch of phase-separated states. This is expected in accordance with analyses of the relation between bifurcation diagrams for finite domains and phase diagrams (thermodynamic limit) performed for Cahn-Hilliard and PFC models in Ref. [41]. Increasing the domain size would in Fig. 6 (a) result in a nearly horizontal branch of stable phase-separated states limited by saddle-node bifurcations that approach the binodal values. This confirms also for the present model that the branch of phase-separated states corresponds to a finite-domain representation of the gas-liquid coexistence and may be taken as an indication of a first order transition.

At the supercritical bifurcation at $\bar{\phi} \approx -0.251$ a branch of domain-filling periodic states (with $n = 18$ peaks, dark blue line) emerges from the uniform state. However, shortly thereafter, another supercritical pitchfork bifurcation at $\bar{\phi} \approx -0.239$ results in another branch of domain-filling periodic states, this time with $n = 19$ peaks. The $n = 18$ branch is initially stable but is already at $\bar{\phi} \approx -0.249$ destabilized in a secondary pitchfork bifurcation. There, two branches of localized states (LSs) emerge subcritically – one with an odd ($\mathrm{LS}_{\mathrm{odd}}$) and one with an even ($\mathrm{LS}_{\mathrm{even}}$) number of peaks (orange lines). Both are initially unstable, at first closely approach and then follow the branch of the stable phase-separated states till beyond its maximum. The corresponding profiles resemble phase-separated states with an additional distinct small-scale periodic modulation of the high-density plateau. In other words, a patch of weakly crystalline state coexists with a gaseous background, for an example see panel II of Fig. 4. Both branches of LSs fold back toward larger $\bar{\phi}$ in saddle-node bifurcations at $\bar{\phi} \approx -1.9$. There, the $\mathrm{LS}_{\mathrm{odd}}$-branch is stabilized, while the $\mathrm{LS}_{\mathrm{even}}$-branch remains unstable (one unstable eigenvalue) till it is stabilized in a further pitchfork bifurcation, where a short branch of asymmetric LSs emerges subcritically (first short green branch). A typical asymmetric state can be seen in panel IV of Fig. 4. In total, 27 such branches connect the $\mathrm{LS}_{\mathrm{odd}}$-branch and the $\mathrm{LS}_{\mathrm{even}}$-branch together forming snake-and-ladder structures of slanted homoclinic snaking typical for systems with a conservation law, i.e., when the mean density is employed as control parameter [39, 40, 43]. In contrast, if the chemical potential were used as control parameter the snaking would become vertically aligned (cf. Fig. 6 (a) when rotated by 90 degree and the discussions in [39, 40]).

Inspection of the energies in Fig. 5 shows that the two branches of symmetric LSs (that correspond to gas-solid coexistence) alternatingly form the global minimum between $\bar{\phi} \approx -1.829$ and $\bar{\phi} \approx 0.103$. In this range there is always at least one stable LS and the two branches of symmetric LSs exchange stability via the asymmetric runge states.

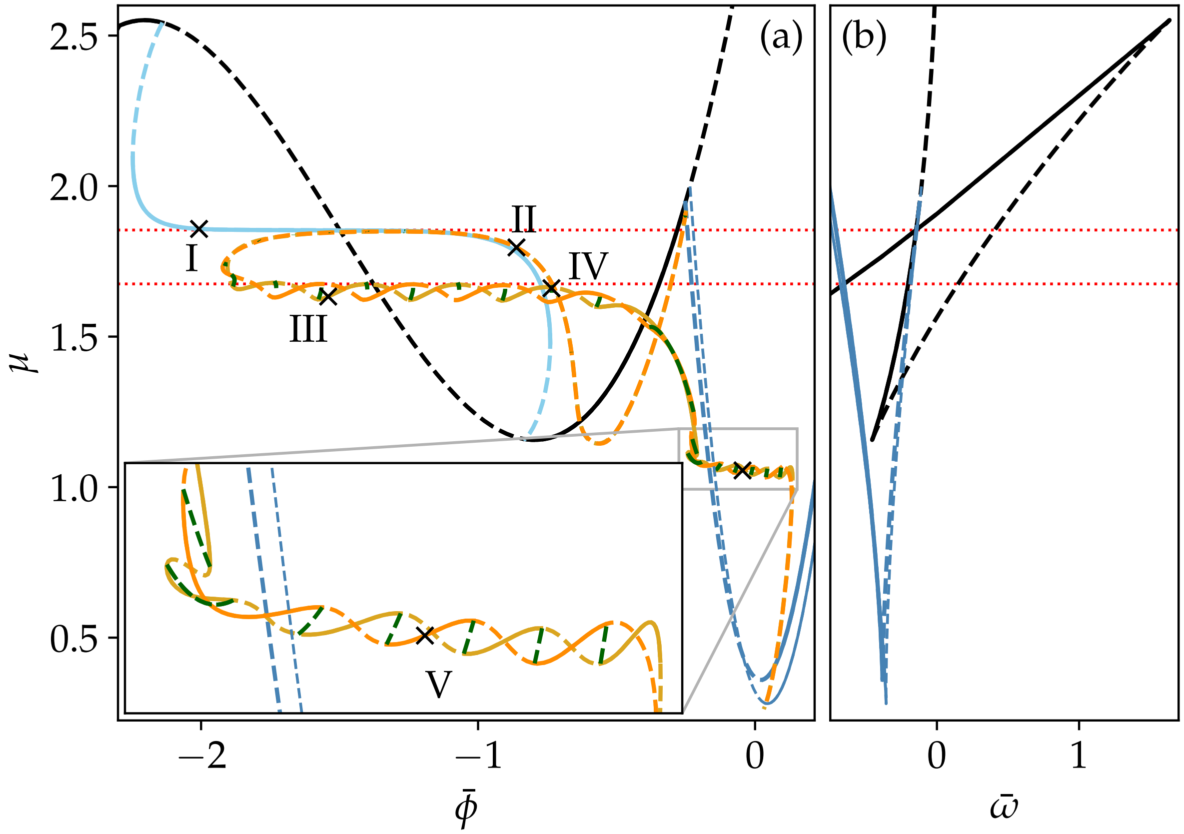

FIG. 6. Panels (a) and (b) give the chemical potential μ as a function of the mean density $\bar{\phi}$ and of the mean grand potential $\bar{\omega}$, respectively, for the passive case in Fig. 4. In (b), for clarity, only branches of domain-filling states are included. Intersections of branches of stable states (solid lines) indicate Maxwell (binodal) points. The corresponding states coexist in the thermodynamic limit and are marked by filled circles in Fig. 4. The horizontal red dotted lines indicate the chemical potential of the pairs of binodal points. Note that at $\mu \approx 1.2$ there is almost another such intersection in (b) causing the snaking of branches magnified in the inset of (a). The indicated stabilities correspond to control parameter $\bar{\phi}$, i.e., the stability with respect to perturbations at fixed $\bar{\phi}$ (and adapting μ). All parameters, line styles and symbols are as in Fig. 4.

Further, it is discernible that the energy of the subcritical, i.e., unstable part of the branches of symmetric LS (the orange lines close to the blue lines in Fig. 4) is slightly larger than the energy of the linearly stable phase-separated states. This indicates that the former represent the threshold states that have to be overcome to reach the stable LS of lowest energy from the metastable phase-separated state. While panels III and IV of Fig. 4 are relatively close to solid-liquid-gas coexistence (in 1D the triple point is at $(\bar{\phi}, T) \approx (-0.379, -0.271)$) and show "liquid shoulders" between the gas and the crystal phase, state V is a clear liquid-solid coexistence.

Fig. 6 (a) actually shows two distinct snaking structures, one at $\mu \approx 1.676$ [related to the just discussed gas-solid coexistence that is indicated by the crossing of the black and blue solid lines in Fig. 6 (b)], and another one at $\mu \approx 1.06$ [magnified in the inset of Fig. 6 (a)], related to the near liquid-solid coexistence that is in Fig. 6 (b) indicated by the near touching of the saddle-node bifurcation where solid and dashed black lines meet, and the blue solid line. One may say that this liquid-solid coexistence is due to a "ghost-binodal" because the branches come very close to each other without actually crossing. Coexistence is indicated by thin horizontal lines in Fig. 6 (a) that are decorated by horizontally aligned branches and snaking structures. In Fig. 4 the second snaking structure occurs in the vicinity of the locus of profile V. Note that the two parts of the branches of LSs where the two snaking structures respectively occur are separated by a further pair of saddle-node bifurcations on the $\mathrm{LS}_{\mathrm{odd}}$-branch [$\mathrm{LS}_{\mathrm{even}}$]-branch at $\bar{\phi} \approx -0.218$ and $\bar{\phi} \approx -0.230$ [$\bar{\phi} \approx -0.210$ and $\bar{\phi} \approx -0.243$]. Finally, when the LSs have filled the entire finite domain the branches of LSs end in pitchfork bifurcations on the branch of domain-filling crystal states with $n = 19$ peaks. At large densities above $\bar{\phi} \approx 0.103$, the domain-filling crystal with $n = 19$ corresponds to the state of lowest energy (Fig. 5). Overall, one may say that the bifurcation structure combines structures known from CH and PFC models in a way as one would expect in the vicinity of a gas-liquid-crystal triple point, and also shows the expected relation to the phase

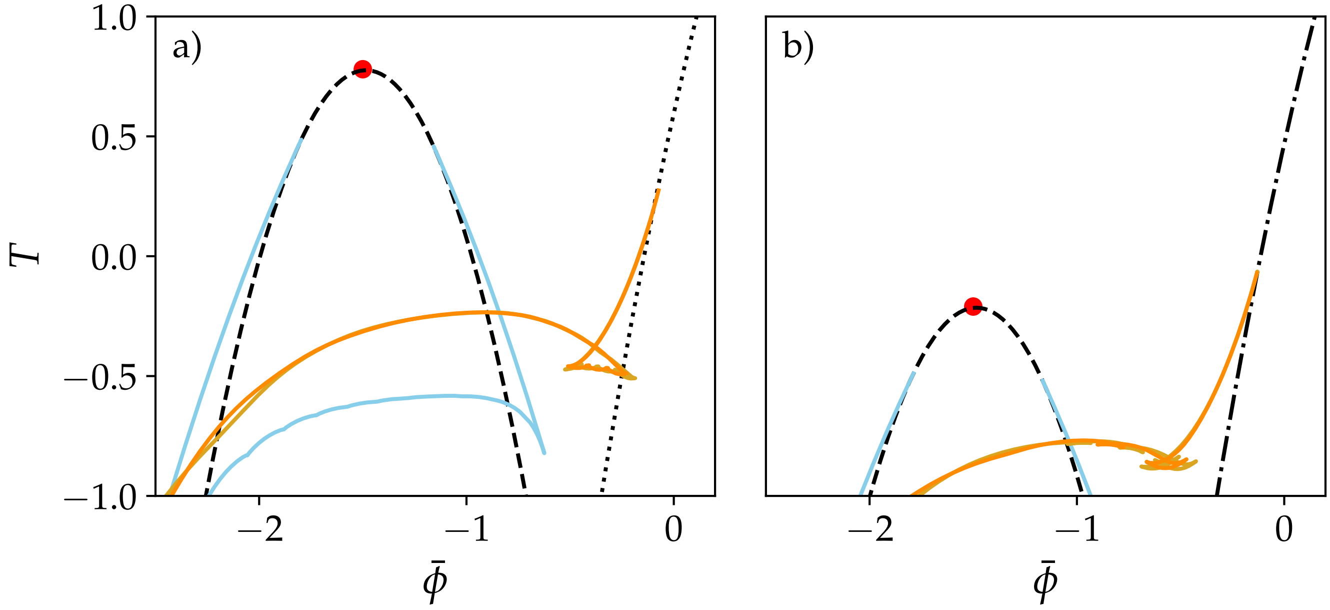

FIG. 7. Loci of saddle-node bifurcations in the PFC Model Eqs. (1) and (2) at (a) $v_0 = 0$, $\zeta = 0$ and (b) $v_0 = 1$, $\zeta = 0$. Shown are the loci resulting from two-parameter continuations in T and $\bar{\phi}$. In case of the yellow and orange branches only the outermost folds for stationary states are tracked. Black dashed and dotted lines denote the spinodal lines for Cahn-Hilliard and conserved-Turing instabilities respectively, while the dot-dashed lines indicate a conserved-wave instability. The red dot marks the critical point of the gas-liquid spinodal. The remaining parameters as in Table I, while the domain size and colors are is as in Fig. 4

diagram.

Finally, we briefly discuss how main features of the bifurcation structure change when including activity. To this end we revisit Fig. 1 of the SM for a system of finite size L = 100, i.e., the spinodals are slightly shifted, see Fig. 7. Additionally, we track the outermost saddle-node (and primary pitchfork) bifurcations of branches of steady phase-separated and localized crystallite states in the $(\bar{\phi}, T)$-plane. They represent good finite-domain approximations of binodals, see [41]. The resulting loci for the gas-liquid coexistence are shown in light blue and branch off from the spinodal representing the Cahn-Hilliard instability. The remaining colored lines represent the loci of the outermost saddle-node bifurcations for the branches of localized states of odd (orange) and even (yellow) number of peaks. They are nearly on top of each other and represent the complexities of the bifurcation structure as discussed above. Additional traveling states exist in (b) and (c) (not shown) but do not have a significant impact on the overall size of the coexistence region. The orange/yellow swallow tail structure marks the region where the triple point is located. The different parts of the orange line are related to the different coexistences with the crystal state (including metastable pairings).

Overall, adding the density-independent velocity lowers not only the gas-liquid spinodal (and critical point marked by the red dot) and associated binodals, but also the binodal related to crystallization. Adding a density-dependent velocity, however, counters this effect, and moves up the gas-liquid spinodal and binodals, but also (to a lesser extent) the liquid-solid binodal. This corresponds to motility-enhanced phase separation and motility-enhaned crystallization.

---

[*] max.holl@aalto.fi; ORCID ID: 0000-0001-6451-9723; M.H. and A.S. contributed equally to this work.
[†] a_stei52@uni-muenster.de; ORCID ID: 0000-0001-6598-9700; MH and AS contributed equally to this work.
[‡] tevrugtm@uni-mainz.de; ORCID ID: 0000-0002-1139-3925
[§] u.thiele@uni-muenster.de; http://www.uwethiele.de; ORCID ID: 0000-0001-7989-9271

[1] A. M. Menzel and H. Löwen. Traveling and resting crystals in active systems. *Phys. Rev. Lett.*, 110:055702, 2013. `doi:10.1103/PhysRevLett.110.055702`.
[2] L. Ophaus, J. Kirchner, S. V. Gurevich, and U. Thiele. Phase-field-crystal description of active crystallites: Elastic and inelastic collisions. *Chaos*, 30:123149, 2020. `doi:10.1063/5.0019426`.
[3] H. Emmerich, H. Löwen, R. Wittkowski, T. Gruhn, G. I. Tóth, G. Tegze, and L. Gránásy. Phase-field-crystal models

for condensed matter dynamics on atomic length and diffusive time scales: an overview. *Adv. Phys.*, 61:665–743, 2012. doi:10.1080/00018732.2012.737555.

[4] A. J. Archer, D. J. Ratliff, A. M. Rucklidge, and P. Subramanian. Deriving phase field crystal theory from dynamical density functional theory: Consequences of the approximations. *Phys. Rev. E*, 100:022140, 2019. doi:10.1103/PhysRevE.100.022140.

[5] Z.-L. Wang, Z. Liu, Z.-F. Huang, and W. Duan. Minimal phase-field crystal modeling of vapor-liquid-solid coexistence and transitions. *Phys. Rev. Materials*, 4:103802, 2020. doi:10.1103/PhysRevMaterials.4.103802.

[6] L. Ophaus, E. Knobloch, S. V. Gurevich, and U. Thiele. Two-dimensional localized states in an active phase-field-crystal model. *Phys. Rev. E*, 103:032601, 2021. doi:10.1103/PhysRevE.103.032601.

[7] T. Speck, J. Bialké, A. M. Menzel, and H. Löwen. Effective Cahn-Hilliard equation for the phase separation of active Brownian particles. *Phys. Rev. Lett.*, 111:218304, 2014. doi:10.1103/PhysRevLett.112.218304.

[8] J. Bialké, H. Löwen, and T. Speck. Microscopic theory for the phase separation of self-propelled repulsive disks. *EPL*, 103:30008, 2013. doi:10.1209/0295-5075/103/30008.

[9] P. Romanczuk, M. Bär, W. Ebeling, B. Lindner, and L. Schimansky-Geier. Active Brownian particles from individual to collective stochastic dynamics. *Eur. Phys. J.-Spec. Top.*, 202:1–162, 2012. doi:10.1140/epjst/e2012-01529-y.

[10] M. E. Cates and J. Tailleur. Motility-induced phase separation. *Annu. Rev. Condens. Matter Phys.*, 6:219–244, 2015. doi:10.1146/annurev-conmatphys-031214-014710.

[11] G. S. Redner, M. F. Hagan, and A. Baskaran. Structure and dynamics of a phase-separating active colloidal fluid. *Phys. Rev. Lett.*, 110:055701, 2013. doi:10.1103/PhysRevLett.110.055701.

[12] L. Caprini, U. M. B. Marconi, and A. Puglisi. Spontaneous velocity alignment in motility-induced phase separation. *Phys. Rev. Lett.*, 124:078001, 2020. doi:10.1103/PhysRevLett.124.078001.

[13] Z. T. Liu, Y. Shi, Y. Zhao, H. Chaté, X.-q. Shi, and T. H. Zhang. Activity waves and freestanding vortices in populations of subcritical Quincke rollers. *Proc. Natl. Acad. Sci. U.S.A.*, 118:e2104724118, 2021. doi:10.1073/pnas.2104724118.

[14] M. te Vrugt, H. Löwen, and R. Wittkowski. Classical dynamical density functional theory: From fundamentals to applications. *Adv. Phys.*, 69:121–247, 2020. doi:10.1080/00018732.2020.1854965.

[15] S. Hermann, P. Krinninger, D. de las Heras, and M. Schmidt. Phase coexistence of active Brownian particles. *Phys. Rev. E*, 100:052604, 2019. doi:10.1103/PhysRevE.100.052604.

[16] R. Wittkowski, J. Stenhammar, and M. E. Cates. Nonequilibrium dynamics of mixtures of active and passive colloidal particles. *New J. Phys.*, 19:105003, 2017. doi:10.1088/1367-2630/aa8195.

[17] M. te Vrugt, J. Bickmann, and R. Wittkowski. How to derive a predictive field theory for active Brownian particles: a step-by-step tutorial. *J. Phys.: Condens. Matter*, 35:313001, 2023. doi:10.1088/1361-648X/acc440.

[18] J. Bickmann and R. Wittkowski. Predictive local field theory for interacting active Brownian spheres in two spatial dimensions. *J. Phys.: Condens. Matter*, 32(21):214001, 2020. doi:10.1088/1361-648x/ab5e0e.

[19] M. te Vrugt and R. Wittkowski. Relations between angular and Cartesian orientational expansions. *AIP Adv.*, 10:035106, 2020. doi:10.1063/1.5141367.

[20] U. Marini Bettolo Marconi and P. Tarazona. Dynamic density functional theory of fluids. *J. Chem. Phys.*, 110:8032–8044, 1999. doi:10.1063/1.478705.

[21] A. J. Archer and R. Evans. Dynamical density functional theory and its application to spinodal decomposition. *J. Chem. Phys.*, 121:4246–4254, 2004. doi:10.1063/1.1778374.

[22] J. Jeggle, J. Stenhammar, and R. Wittkowski. Pair-distribution function of active Brownian spheres in two spatial dimensions: simulation results and analytic representation. *J. Chem. Phys.*, 152, 2020. doi:10.1063/1.5140725.

[23] S. Bröker, M. te Vrugt, J. Jeggle, J. Stenhammar, and R. Wittkowski. Pair-distribution function of active Brownian spheres in three spatial dimensions: simulation results and analytical representation. *Soft Matter*, 20:224–244, 2024. doi:10.1039/D3SM00987D.

[24] S. Bröker, M. te Vrugt, and R. Wittkowski. Collective dynamics and pair-distribution function of active Brownian ellipsoids in two spatial dimensions. *Commun. Phys.*, 7:238, 2024. doi:10.1038/s42005-024-01674-x.

[25] A. J. M. Yang, P. D. Fleming, and J. H. Gibbs. Molecular theory of surface tension. *J. Chem. Phys.*, 64:3732–3747, 1976. doi:10.1063/1.432687.

[26] M. te Vrugt, M. P. Holl, A. Koch, R. Wittkowski, and U. Thiele. Derivation and analysis of a phase field crystal model for a mixture of active and passive particles. *Modelling Simul. Mater. Sci. Eng.*, 30:084001, 2022. doi:10.1088/1361-651X/ac856a.

[27] Z.-F. Huang, M. te Vrugt, R. Wittkowski, and H. Löwen. Active pattern formation emergent from single-species nonreciprocity. *arXiv:2404.10093*, 2024. doi:10.48550/arXiv.2404.10093.

[28] In Ref. [27] this corresponds to the parameter B_1, the relation is $B_1 = \zeta/2$.

[29] Z.-F. Huang, M. te Vrugt, R. Wittkowski, and H. Löwen. Anomalous grain dynamics and grain locomotion of odd crystals. *arXiv:2505.03957*, 2025. doi:10.48550/arXiv.2505.03957.

[30] J. Toner and Y. Tu. Long-range order in a two-dimensional dynamical XY model: how birds fly together. *Phys. Rev. Lett.*, 75:4326, 1995. doi:10.1103/PhysRevLett.75.4326.

[31] T. Frohoff-Hülsmann and U. Thiele. Nonreciprocal Cahn-Hilliard model emerges as a universal amplitude equation. *Phys. Rev. Lett.*, 131:107201, 2023. doi:10.1103/PhysRevLett.131.107201.

[32] D. Greve and U. Thiele. An amplitude equation for the conserved-Hopf bifurcation – derivation, analysis and assessment. *Chaos*, 34:123134, 2024. doi:10.1063/5.0222013.

[33] F. Turci and N. B. Wilding. Phase separation and multibody effects in three-dimensional active Brownian particles. *Phys. Rev. Lett.*, 126:038002, 2021. doi:10.1103/PhysRevLett.126.038002.

[34] A. K. Omar, K. Klymko, T. GrandPre, and P. L. Geissler. Phase diagram of active Brownian spheres: crystallization and the metastability of motility-induced phase separation. *Phys. Rev. Lett.*, 126:188002, 2021. `doi:10.1103/PhysRevLett.126.188002`.

[35] L. Ophaus. *Analysis of the Active Phase-Field-Crystal Model.* PhD thesis, Westfälische Wilhelms-Universität Münster, Münster, 2019.

[36] J. P. Boyd. *Chebyshev and Fourier spectral methods.* Dover Publ., Mineola, NY, 2. (rev.) edition, 2001.

[37] S. Engelnkemper, S. V. Gurevich, H. Uecker, D. Wetzel, and U. Thiele. Continuation for thin film hydrodynamics and related scalar problems. In A. Gelfgat, editor, *Computational Modeling of Bifurcations and Instabilities in Fluid Mechanics*, Computational Methods in Applied Sciences, vol 50, pages 459–501. Springer, Cham, 2019. `doi:10.1007/978-3-319-91494-7_13`.

[38] H. Uecker, D. Wetzel, and J. D. M. Rademacher. pde2path - a Matlab package for continuation and bifurcation in 2D elliptic systems. *Numer. Math.-Theory Methods Appl.*, 7:58–106, 2014. `doi:10.4208/nmtma.2014.1231nm`.

[39] U. Thiele, A. J. Archer, M. J. Robbins, H. Gomez, and E. Knobloch. Localized states in the conserved Swift-Hohenberg equation with cubic nonlinearity. *Phys. Rev. E*, 87:042915, 2013. `doi:10.1103/PhysRevE.87.042915`.

[40] M. P. Holl, A. J. Archer, S. V. Gurevich, E. Knobloch, L. Ophaus, and U. Thiele. Localized states in passive and active phase-field-crystal models. *IMA J. Appl. Math.*, 86:896–923, 2021. `doi:10.1093/imamat/hxab025`.

[41] U. Thiele, T. Frohoff-Hülsmann, S. Engelnkemper, E. Knobloch, and A. J. Archer. First order phase transitions and the thermodynamic limit. *New J. Phys.*, 21:123021, 2019. `doi:10.1088/1367-2630/ab5caf`.

[42] M. P. Holl, A. J. Archer, and U. Thiele. Efficient calculation of phase coexistence and phase diagrams: Application to a binary phase-field crystal model. *J. Phys.: Condens. Matter*, 33:115401, 2021. `doi:10.1088/1361-648X/abce6e`.

[43] E. Knobloch. Localized structures and front propagation in systems with a conservation law. *IMA J. Appl. Math.*, 81:457–487, 2016. `doi:10.1093/imamat/hxw029`.